A model for dislocation creep in polycrystalline Ni-base superalloys at intermediate temperatures

E.I. Galindo-Nava [a,b,*], R. Schlütter [b], O.M.D.M. Messé [c], C. Argyrakis [d], C.M.F. Rae [b]

[a] Department of Mechanical Engineering, University College London, Torrington Place, London, WC1E 7JE, UK
[b] Department of Materials Science and Metallurgy, University of Cambridge, 27 Charles Babbage Rd, Cambridge, CB3 0FS, UK
[c] Oerlikon AM Europe GmbH, Kapellenstr. 12, Feldkirchen, 85622, Germany
[d] Rolls-Royce plc, PO Box 31, Derby, DE24 8BJ, UK

ARTICLE INFO

ABSTRACT

A model for creep at intermediate temperatures in polycrystalline Ni-based superalloys is presented. The model is based on describing stacking fault nucleation, propagation and subsequent shear within the γ matrix and γ' precipitates. The critical energy for stacking fault nucleation is obtained by minimising the energy to form a stacking fault from dislocation partials, which is promoted by local stress concentrations. The extent of stacking fault shear at a γ' precipitate is estimated using a force balance at the γ/γ' interface to determine the critical shear distance The model results are validated against creep experimental data in several polycrystalline superalloys showing good agreement. Individual contributions to creep from key microstructural features, including grain size and γ' distribution, are studied to identify which ones are more significant. Similarly, it is shown that one of the main factors controlling the creep rate is the stacking fault energy in the γ as it dictates the stacking fault nucleation and shear rates. Parameter analysis on alloying additions typically used in commercial superalloys demonstrates which elements have the strongest effect on creep, highlighting how the present model can be used as tool for alloy and microstructure design against dislocation creep.

1. Introduction

Polycrystalline nickel-base superalloys are widely employed in hot parts of gas turbine engines due to their good mechanical properties at high temperatures. Their hot strength stems from the precipitation of γ' (L1$_2$) particles in a solution-strengthened face-centred cubic matrix (γ). The γ' particles can hold multimodal size distributions, including intragranular secondary γ', of 100–300 nm in size, and tertiary γ', of 15–75 nm in size. Improving the performance of turbine discs requires increasing the creep resistance of polycrystalline superalloys at intermediate temperatures in excess of 650 °C and up to 800 °C, where dislocation creep is active. It is well established in that stacking fault shear followed by microtwinning controls dislocation creep deformation within the temperature range 650–800 °C and at high applied stresses (but below the yield point). For instance, Smith et al. (2006) developed a creep mechanism map in René 104 highlighting that stacking fault shear operates primarily between 650–900 °C and ≤ 800 MPa; other authors have reported that stacking fault shear is the dominant creep deformation in polycrystalline superalloys under similar deformation conditions (Kovarik et al., 2009; Smith et al., 2006). Similarly, it has been reported that primary creep in single-crystal superalloys below 800 °C and between 400–900 MPa is controlled by stacking fault shearing and microtwinning (Reed, 2006; Barba et al., 2017; Bonnet and Ati, 1991; Rae and Reed, 2007).

Although there is empirical understanding of creep at intermediate temperatures (650 °C–800 °C) in polycrystalline superalloys, there is virtually no predictive physics-based model able to capture the underlying mechanisms and their associated effects in creep strain. Models for creep in superalloys have been proposed but they are based on different dislocation-based mechanisms above 800 °C, for instance dislocation recovery (Svoboda and Lukáš, 1997; Pollock and Argon, 1992) and climb around γ' precipitates (Dyson, 2009; Zhu et al., 2012). In addition, most microstructure-sensitive models for creep in superalloys have been proposed with focus mainly being on single-crystal alloys at higher temperatures. For instance, continuum approaches combining phase-field and dislocation dynamics have been developed to study dislocation and microstructure evolution in high temperature creep ($\geq 1000\,°C$) (Wu et al., 2017; Wu and Zhang, 2022). Svoboda and Lukáš (1997), Svoboda and Lukáš (1998, 2000) proposed a constitutive model considering several mechanisms, including dislocation slip in γ and γ', dynamic recovery and morphological changes of the (cuboidal) γ' particles leading to rafting, however, their model did not consider stacking fault evolution and the γ/γ' morphology considered is not applicable to polycrystalline superalloys. Models based on dislocation dynamics have been adopted to study primary creep controlled by dislocation looping around cuboidal precipitates (Zhao et al., 2018; Chang et al., 2018; Chatterjee et al., 2021), as well as diffusion-assisted plasticity (Barba et al., 2018). Models for high temperature creep ($\geq 800\,°C$) in polycrystalline alloys have also been proposed. For instance, power-law models to predict secondary and tertiary creep rates of Inconel 718 have been postulated based on changing the stress exponents with precipitate coarsening (Drexler et al., 2018; Becker and Hackenberg, 2011). Numerical semi-empirical models have been derived by Kim et al. (2016, 2018) to study the effect of the microstructure on creep controlled by Orowan looping. Although good understanding and predictability has been obtained in the previous works, to the authors knowledge, no approach has succeeded in capturing creep in polycrystalline alloys at temperatures between 600 °C–800 °C which is primarily controlled by stacking fault shearing. Moreover, effects of chemical composition on creep deformation, *e.g.* via changing surface energies, have not been explored in existing models. A main reason for the lack of a stacking fault shear-based creep model is the difficulty in isolating the effects of the microstructure and chemical composition on stacking fault formation and propagation in both the γ and γ' phases. Another reason is that the power-law creep equation is known to breakdown in the region where dislocation creep operates, *i.e.* at intermediate temperatures ($0.3T_m \leq T \leq 0.3T_m$) and high stress levels (Nabarro, 2004). We have shown in previous work that the strain controlled by dislocation creep in single-phase FCC alloys can be predicted using a square root of time expression to describe dislocation glide (Galindo-Nava and Rae, 2016). This equation was derived considering a combined mechanism of atom diffusion and cross-slip controlling screw dislocation motion during creep at this temperature range. In addition, dislocation creep in polycrystalline superalloys is known to be governed mainly by primary and tertiary creep, whereas secondary (steady-state) creep is sometimes absent (Kovarik et al., 2009). This implies that power-law creep is not applicable in the present case, hence a new modelling framework is needed.

Stacking faults form in the γ and propagate through grain interiors, cutting the tertiary and secondary γ' particles as the creep strain progresses. Microtwinning is activated once sufficient stacking faults form along the grain interiors but it is also known that the structure of the γ' can delay its activation (Kovarik et al., 2009). In addition, the chemical composition influences greatly the creep rate in superalloys in a complex fashion. Amongst typical elements used in commercial alloys, Co has the strongest effect without modifying the microstructure by reducing the stacking fault energy in the γ and γ' (Zhi'an et al., 1988; Cui et al., 2011; Jones et al., 2014). W, Mo, and Cr increase the creep life by solid solution strengthening in the γ but can also affect the stacking fault energy (Rae and Zhang, 2009; Zhang et al., 2010). Ta, Nb and Ti additions increase the creep life at intermediate temperatures by strengthening the γ' and making it more difficult to shear (Huron et al., 2008; Reed, 2006; Meng et al., 1984). Moreover, the chemical composition not only affects the fault energies and solution hardening effects but it has been shown extensively that elemental segregation is necessary to form complex stacking faults at temperatures in excess of 300 °C (Koizumi et al., 2011, 2012; Kamino et al., 1992). Co, Cr and Mo tend to segregate to stacking faults in both the γ (Han et al., 2003; Koizumi et al., 2012) and γ' (Viswanathan et al., 2015).

The objective of the present work is to introduce a physics-based model for creep in superalloys describing the main mechanisms leading to stacking fault shearing and twinning. The model is based on describing the sequential evolution of stacking fault shearing by first predicting stacking fault formation in the γ, then performing a force balance at the γ/γ' interface to estimate the critical resolved shear stress and finally establishing the propagation rate in terms of short term atomic diffusion. It is shown that one of the main parameters controlling the creep rate is the stacking fault energy in the γ as it dictates the stacking fault nucleation rate. The model predictions are validated against experimental data from several polycrystalline superalloys showing good agreement in most cases, where individual contributions from the microstructure are studied, *i.e.* grain size and γ' size and volume fraction. Similarly, effects of chemical composition on creep life are explored showing how the present model can be used as tool for alloy design against creep. The present model is applicable in the region of power-law breakdown, which occurs at stresses above dislocation climb and below dislocation slip at plastic yielding. However, it reaches its limit towards higher temperatures when dislocation climb may be dominant or lower stresses where grain-boundary sliding and other diffusion processes may operate.

2. Materials and methods

The model is tested against experimental data in eight superalloys containing unimodal and multimodal γ' size distributions. Creep tests were conducted for RR1000 and the remaining data were obtained from the literature. Table 1 shows the nominal composition of the commercial alloys referred to in this work. Udimet 720Li in Cui et al. (2012) and Tian et al. (2014) has been referred to as NiSup2. No carbides, interstitial elements or substitutional elements with concentrations less than 0.5 wt% are considered, since their contribution to stacking fault shear and stacking fault energy are low (Reed, 2006).

Table 1
Chemical composition in wt% of superalloys tested.

Alloy	Ni	Co	Cr	Mo	W	Fe	Al	Ti	Nb	Ta	Author
RR1000	Bal.	18.5	15	5	–	–	3	3.6	–	2	this work, Connor (2009)
Allvac 718plus	Bal.	9.1	17.4	2.72	1.04	9.66	1.46	0.71	5.48	–	Hayes et al. (2015)
NiSup1	Bal.	5	16.3	3.1	1.3	–	2.4	4.8	–	–	Cui et al. (2012), Tian et al. (2014)
Udimet 720Li (NiSup2)	Bal.	15	16.3	3.1	1.3	–	2.4	4.8	–	–	Cui et al. (2012), Tian et al. (2014), Jackson and Reed (1999)
NiSup3	Bal.	23	16.3	3.1	1.3	–	2.4	4.8	–	–	Cui et al. (2012), Tian et al. (2014)
René 88DT	Bal.	13	16	4	4	–	2.1	3.7	0.7	–	Viswanathan et al. (2005)
ME3	Bal.	20.6	11	3.7	2	–	3.4	3.6	0.9	2.4	Smith et al. (2006)
TMW-4M3	Bal.	13.5	25	2.8	1.2	–	2.3	6.2	–	–	Yuan et al. (2011a)
TMW-2	Bal.	14.4	21.8	2.7	1.1	–	2.3	6.2	–	–	Yuan et al. (2011a)
MC2	Bal.	8	5	2	8	–	5	1.5	–	6	Benyoucef et al. (1995), Legros et al. (2002)

Coarse-grained RR1000, forged to a disc shape at subsolvus temperature and subsequently heat treated at 1170 °C/2 h/fan air cool and 760 °C/16 h/static air cool, was provided by Rolls-Royce plc. The microstructure generated is referred to as typical. Material was extracted from the bore of the disc and machined to dog-bone shaped samples with 48 mm overall and 25 mm gauge length of 3.19 mm diameter. In order to assess the influence of γ' size on the creep behaviour, a proportion of the samples were given an additional heat treatment. To reduce surface oxidation, these were wrapped in tantalum foil and encapsulated in quartz tubes filled with argon. The heat treatment consisted of solutioning at 1180 °C/2 h/water quench and ageing at 860 °C/1 h/water quench aiming for small γ' precipitates. This is referred to as the "fine" microstructure.

For microstructural examination via scanning electron microscopy (SEM), samples were ground with successively finer paper up to 4000 grade, then polished with 1 μm and 0.25 μm diamond suspension and lastly polished with OPS at 10 N per sample with an automatic polisher. The samples were suspended in Kallings reagent for 20 s to etch away γ' precipitates. For transmission electron microscopy (TEM) characterisation, 150–200 μm thick slices were cut, spark eroded to 3 mm diameter discs and hand polished to under 180 nm thickness. Electropolishing in a Struers Tenupol-5 jet polisher at 19 V using 6% perchloric acid in methanol at -5 °C $\pm$ 1 °C generated a hole with electron-transparent edges within the samples.

2.1. Microscopy

The characterisation of γ' sizes in the fine microstructure was conducted via SEM and TEM. Secondary γ' measurements relied on SEM micrographs taken via back-scattered electrons at 6 mm working distance and 15 kV in immersion mode with a FEI Nova NanoSEM FEG. The precipitate distribution was analysed via ImageJ and Matlab using manual thresholding, removal of outliers smaller than 5 pixels, despeckling and watershedding. Assuming circular precipitates to calculate diameters then allowed fitting of a log-normal distribution with a significantly improved fit achieved through a 60 nm minimum size threshold. Tertiary γ' characterisation is based on TEM micrographs taken at 200 kV via a FEI Tecnai Osiris 80–200 or a FEI Tecnai F20 FEGTEM. Precipitate outlines were traced manually, based on micrographs taken in the thinnest sections of the samples. Outlines were then analysed using ImageJ assuming circular particles. The typical microstructure, including grain size distribution was characterised in Messe (2015). Fig. 1(a) shows an overview of the grain structure obtained for the typical microstructure. A log-normal grain size distribution of $15.7^x/2.0$ μm was found in case of twins identified as separate grains, otherwise it resulted in a $25.6^x/2.0$ μm distribution. The grain size was assumed to be identical in both microstructures. This is because Collins and Stone (2014) conducted similar solutionising heat treatments in RR1000 at 1170 °C and 1180 °C and found that the final grain size in both conditions is constant at ~ 25 μm, which is similar to the one measured in the present work. This also means that most changes associated to the microstructure correspond only to the secondary and tertiary γ' structure. Fig. 1(b) and (c) show representative micrographs of the typical and fine microstructures, respectively. Within the typical microstructure, secondary γ' shows a $181^x/1.54$ nm distribution and 30 ± 20 nm sized tertiaries. Based on Collins and Stone (2014), the volume fraction of secondary γ' is taken to be 32%, measured also via SEM on coarse-grained RR1000 after a 1170 °C/4 h/oil quench and 760 °C/16 h heat treatment; and 14% volume fraction assumed for tertiary γ', based on an overall determined γ' volume fraction of 46% (Collins and Stone, 2014). The fine microstructure contains of a $93^x/1.22$ nm secondary γ' distribution of 32% volume fraction and 15 ± 4 nm tertiary γ' with also an assumed 14% volume fraction.

2.2. Mechanical testing

High stress creep tests close to the yield stress were conducted on both microstructures. A stress level of 900 MPa was applied to both microstructures, equivalent to around 90% relative yield strength of the fine microstructure. For the tests, an Instron 8501 Low-Cycle Fatigue - 100kN servo hydraulic machine was used equipped with a 3-zone furnace. The tests were stress-controlled, while ramping up to full stress was displacement-controlled with a strain rate of 10^{-2} s^{-1}. K-type thermocouples were attached above and below the load region. Extensometer-facilitated strain measurements could not be gained consistently due to slippage. Therefore, the machine displacement values were divided by the gauge length to obtain consistent strain values. At the end of the tests, the load was set to 250 N and the furnace opened for a fast cool to room temperature. The creep tests were run up to a few strain % and not until failure. This is to focus the study in the regions where stacking fault shear is the dominating deformation mechanism and no damage takes place. This was corroborated by confirming that no damage was present in the specimens after each creep test.
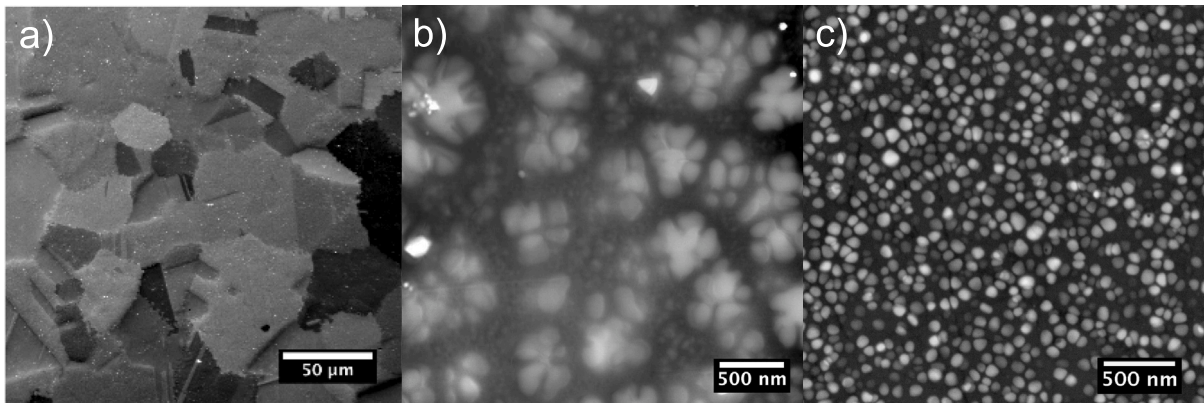
Fig. 1. (a) Grain structure in coarse-grained RR1000. (b) TEM micrographs of typical and (c) fine microstructures.

3. Model derivation

Experimental evidence reported in several superalloys (Reed, 2006; Smith et al., 2006; Rae and Reed, 2007; Barba et al., 2017; Kovarik et al., 2009; Unocic et al., 2008; Viswanathan et al., 2005) indicates that the nucleation and propagation of stacking faults and subsequent shear of γ' precipitates are the dominant creep mechanisms at intermediate temperatures, and the model will be derived based on this assumption. Relevant elements involved stacking fault evolution will be introduced next to later derive the respective equations controlling the creep strain.

Background: Mechanisms controlling stacking fault shear

This section presents the main factors involved in stacking fault shear and twinning which are necessary for a physics-based superalloy creep model. Formation of stacking faults and microtwins is common in FCC metals with low stacking fault energy (γ_{SFE}) (Naeita and Takamura, 1974; Allain et al., 2004). However, the mechanisms of stacking fault formation in superalloys are more complicated due to the presence of the ordered γ' phase and the high alloying content in these materials. Several authors have studied the evolution of stacking fault shear and microtwinning (Viswanathan et al., 2005; Rae and Zhang, 2009; Yuan et al., 2011a, 2012). Their findings can be summarised in the following sequence:

1. Stacking fault nucleation: A preexisting $\frac{1}{2}\langle 110 \rangle$ gliding dislocation in the γ stops at the γ/γ' interface and can dissociate into two $\frac{1}{6}\langle 112 \rangle$ Shockley partials. The dissociation process occurs in the γ as the $\frac{1}{2}\langle 110 \rangle$ dislocation is unable to shear the γ' due to the high energy penalty of forming an anti-phase boundary (Yuan et al., 2012); local stress concentrations build up at the interface which are able to assist the dissociation process. This is schematically shown in Fig. 2(a). In addition, it has been reported that grain boundaries and incoherent precipitates serve as nucleation sites for partial/stacking faults following similar local stress build up due to the local distorted environment (Tschopp and McDowell, 2008; Kienl et al., 2022; Ram et al., 2016; Bauer et al., 2012). We note that in this step it is necessary that a perfect (unit) dislocation forms before the dissociation process can take place.
2. γ' penetration: The newly formed partial leads to the formation of an intrinsic stacking fault embryo that exerts a force on the γ' particles. Once the force is high enough the stacking fault cuts the particle, as shown in Fig. 2(b) and (c), where r^* and l_{SF} represent the critical stacking fault width and length, respectively.
3. γ' shearing: The leading partial enters the γ' forming a complex-stacking fault; while this partial moves through the γ', two Shockley partials nucleate in adjacent (111) planes to form a superlattice extrinsic stacking fault. This mechanism is possible only if local atom reordering, via short range diffusion, occurs to reduce the local strain energy.
4. Stacking fault propagation: As the stacking fault leaves the γ' particle it propagates in the γ, if the stacking fault energy is low enough or if the fraction of γ' is low enough. Fig. 2(c) shows a schematic representation of a stacking fault propagating a distance ΔL_{SF} at a given time. A microtwin forms if additional stacking faults form (steps 1–3) in adjacent {111} planes (Kolbe, 2001; Unocic et al., 2011).

Step 1 is crucial as the ability for partial dislocations to form stacking faults in the γ is the driving process for cutting the γ'. Tian et al. (2014) have studied the effects of the stacking fault energy in the γ on the creep response in superalloys. The Co content was systematically adjusted to tailor specific stacking fault energies, whilst fixing the initial microstructure. They found that the creep life increases as the γ_{SFE} decreases, as well as transitioning from isolated stacking fault shear (in the γ') to extended stacking fault shearing and microtwinning. Other authors have reported similar improvement in the creep life with increasing Co up to ~ 25 wt% (Jarrett and Tien, 1982; Jones et al., 2014; Wang et al., 2015). Moreover, Cui et al. (2012) have shown that γ_{SFE} in the matrix has a significant effect during inverse dynamic strain ageing under tensile deformation; a high stacking fault density was

Table 2
Commercial alloys showing stacking fault shear (SF)/ twinning(T), their stacking fault energy, Co, Cr, Mo and W content in the γ (at%), γ' volume fraction, and deformation temperature.

Alloy	SFE (mJ/m^2)	SF/T	Co	Cr	Mo	W	$f_{\gamma'}$ (%)	T (°C)	Author
RR1000	19.6*	Y	25	28	5	–	45	700	This work
TMW-4M3	19.9	Y	34	27.1	2.5	0.5	48	725	Cui et al. (2011), Yuan et al. (2012)
ME3	21.5*	Y	23	21	4	1	45	650–760	Smith et al. (2006)
TMW-2	23.4	Y	29.8	27.4	2.6	0.6	48	725	Cui et al. (2011), Yuan et al. (2011a)
NiSup3	24.9	Y	31	25	2.9	0.6	45	725	Cui et al. (2012), Tian et al. (2014)
AllVac 718plus	26.4*	Y	11	26	2	0.4	18	691–792	Hayes et al. (2015)
René 88DT	27.7*	Y	15	23	5	2	47	650–750	Viswanathan et al. (2005)
Hastelloy X	27.8*	N	1	24.2	4.4	0.3	0	760	Kim et al. (2011)
MC2	31	Y	9.1	25.9	2.75	4.1	55	800–850	Benyoucef et al. (1995), Legros et al. (2002)
Alloy 263	31.3*	Y	21.1	24.6	3.8	–	10	760	Kim et al. (2011)
U720Li	31.4	Y	20	26	3	0.6	45	450–725	Cui et al. (2012), Tian et al. (2014), Yuan et al. (2011b)
Waspaloy	35.2*	Y	15.5	27	3.3	–	25		Guimier and Strudel (1970)
NiSup1	40.6	Y	7.1	26	2.9	0.6	45	725	Cui et al. (2012), Tian et al. (2014)
Haynes 230	42.9*	Y	0.4	25.3	0.8	4.7	0	760	Kim et al. (2011)
CM247LC	47.7*	Y	16.5	18.9	0.3	3.3	65	760,860	Kim et al. (2011)

reported to promote anomalous strain hardening, indicating that stacking faults are more efficient in accommodating strain. As for step 2, stacking faults are capable of cutting entirely the γ' precipitates (Viswanathan et al., 2005), in spite of most creep tests being held below the critical resolved shear stress to cut a γ' particle by a dislocation pair (Galindo-Nava et al., 2015). The density of stacking faults ρ_{SF} has been reported to increase with temperature up to about 450 °C (Xu et al., 2014), whilst remaining high ($\rho_{SF} \sim 1-5 \times 10^{15}$ m^{-2}) up to 700 °C; the length of the stacking faults typically lies in the range 100–250 nm (Viswanathan et al., 2005; Yuan et al., 2012). The operating mechanisms in Step 3 are the rate-controlling processes for stacking fault propagation, as it is thermally activated due to the short-range diffusion enabling atom segregation to the stacking faults (Kolbe, 2001; Viswanathan et al., 2015). Amongst the typical alloying elements in commercial superalloys, Co, Cr and Mo have been reported to have the strongest effects in the SFE on both the γ (Han et al., 2003; Koizumi et al., 2012) and γ' (Viswanathan et al., 2015).

Following the previous steps, a model describing stacking fault shear and subsequent twinning should contain three components: (1) An equation of the critical conditions for stacking fault formation in the γ as function of the stacking fault energy; (2) a force balance at the γ/γ' interface describing the critical conditions leading to particle cutting and; (3) an equation describing the evolution of the stacking fault/twin density based on their mobility in the γ'. Each item will be derived in the following sections. Item (2) is key to the model derivation and consistent with experimental observations; several authors have indicated that partial dissociation and subsequent particle cutting occurs as consequence of the interacting forces at the γ/γ' interface acting as main mechanisms for strain development (Kovarik et al., 2009; Yuan et al., 2011b; Freund et al., 2017). Another key assumption when developing the models will be that stacking fault shear and microtwinning are treated equally due to the difficulties in characterising their transition; Kovarik et al. (2009) have pointed out that the evolution rate in the γ' of these mechanisms is identical and their dependency on the stacking fault energy is identical (Tian et al., 2014), hence, in principle, the models employed in this work apply to both processes.

Identification of parameters controlling stacking fault shear

The first step is to quantify the values of critical parameters controlling stacking fault evolution within the γ and γ', given the complicated effects of microstructure and composition on creep. This is to identify which have the most significant influence in creep and where they are likely to operate in the previous SF propagation sequence. Table 2 shows relevant parameters in the alloys tested, including: (1) the stacking fault energy in the γ (γ_{SFE}), (2) the Co, Cr, Mo and W content in the matrix, (3) γ' volume fraction in the alloy, and (4) deformation temperature. For the case of the γ–stacking fault energy, experimental values at room temperature using HR–TEM are shown in the table and predicted values using Eq. (15) (see Section 4.1) are shown when no γ_{SFE} measurements have been reported; the latter are denoted by *. The stacking fault energy lies between 19 and 44 mJ m^{-2}, being this range similar to that for deformation twinning activation in austenitic steels (Allain et al., 2004; Galindo-Nava and Rivera-Díaz-del-Castillo, 2017). The third column (SF/T) denotes whether stacking fault shearing and/or microtwinning were reported in the alloys and conditions tested. It is interesting to note that stacking fault shearing operates irrespective of the Co content in the γ, as long as γ_{SFE} is low enough via high additions of Cr+Mo+W in the matrix. Additionally, it is apparent that the γ' volume fraction does not affect the activation of stacking fault shearing and microtwinning, as these structures have also been reported in solid solution alloys (*i.e.* γ'–free Haynes 230) (Kim et al., 2011); however, this behaviour may only hold valid for γ' volume fraction up to $\sim$ 50%, since it is based in empirical reports for polycrystalline superalloys which have less than 50% γ' volume fraction. This corroborates that γ_{SFE} is a main factor controlling creep and that the γ' does not prevent stacking fault shearing/microtwinning but only delays these processes. Additionally, twinning and stacking fault activity have been reported only at the intermediate-temperature range (450–800 °C). This has been confirmed by other authors reporting the absence of stacking fault activity in the same alloys at lower temperatures; for instance, see in Cui et al. (2012) for Udimet 720 Li and in Kim et al. (2011) for Alloy 263, Haynes 230 and CM247LC. Thus, short-range diffusion controls stacking fault propagation in the γ', *i.e.* the overall creep rate.
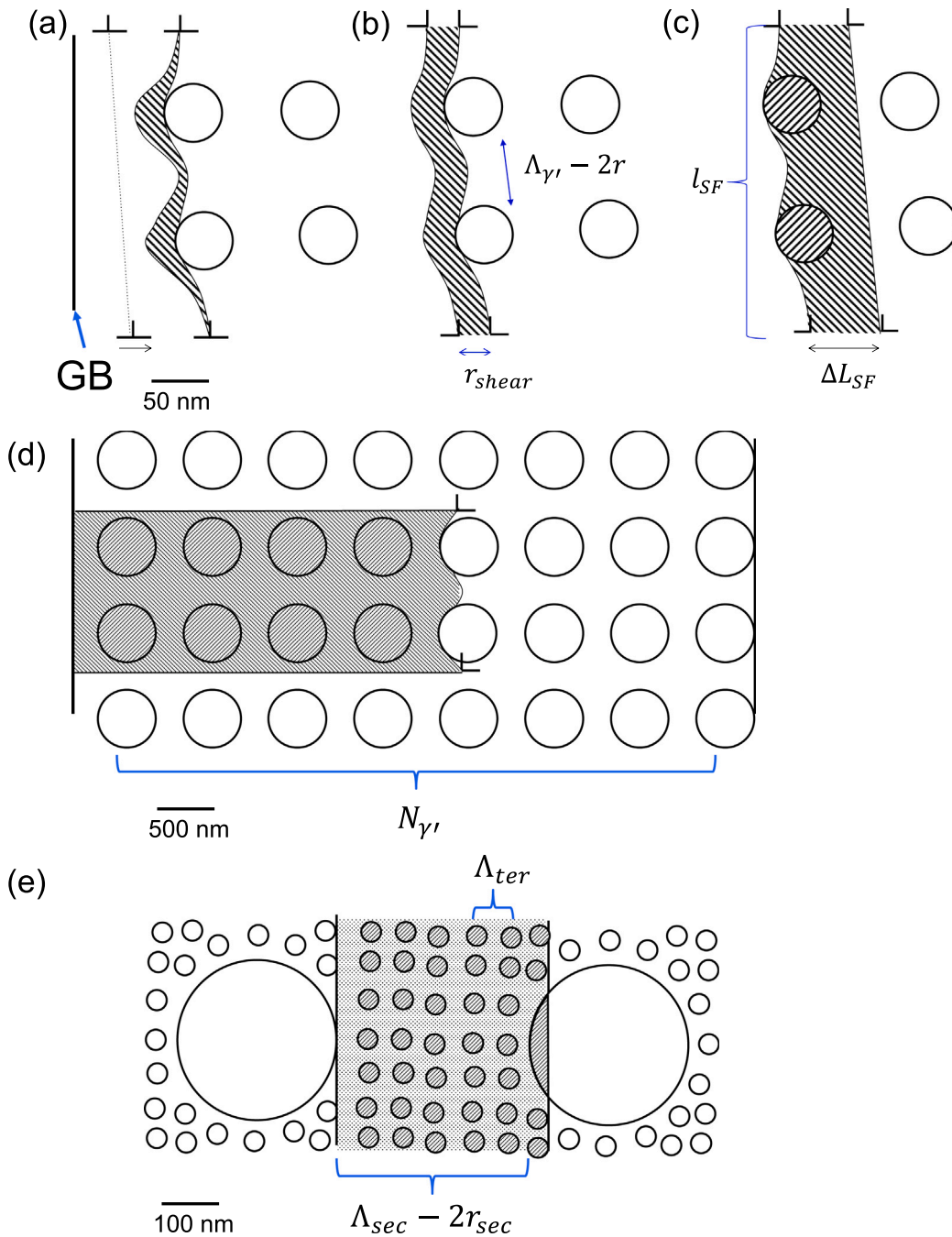
Fig. 2. Schematic representation of a stacking fault shear sequence. (a) Step 1: stacking fault nucleation; (b) Step 2: stacking fault (SF) cutting, (c) Step 3: SF shearing the γ'; and (d) Step 4: SF propagation/twinning. (e) Schematic of bimodal γ' size distribution highlighting additional shear events between secondary γ' particles, depending on the tertiary γ' spacing.

Step 1: Critical energy for stacking fault formation

   A new criterion describing the conditions to nucleate a stacking fault in superalloys is introduced in this section. It is based on a model for twin formation in austenitic steels derived in previous work (Galindo-Nava and Rivera-Díaz-del-Castillo, 2017). The formulation consists in determining the minimum energy involved in the nucleation of a twin embryo in terms of the stacking fault energy and applied stress. The model includes the effects of the stacking fault energy and applied stress in the conditions for twin nucleation. The formulation was also applied to predict ϵ martensite, *i.e.* HCP phase formed by a SF on every other plane.

The critical energy to form a twin E_c is composed by: (*i*) a strain energy term of overlapping dislocations forming the nucleus, $E_{dis} = \frac{n^2 \mu b^2 r}{2\pi(1-\nu)} \ln\left(\frac{r}{2bn^2}\right)$, where $n = 3$ is the number of Shockley partials to form a twin (stacking fault bundles), r is the width of the forming stacking fault, μ is the Shear modulus, b is the Burgers vector, and ν is Poisson's ratio; (*ii*) the energy associated with the nucleation of an embryo, formula derived originally by Olson and Cohen (1976), $E_{emb} = (\gamma_{SFE} - 2\sigma_{HCP})l_{SF}rn$, where σ_{HCP} is the interfacial energy between the faulted and unfaulted regions and l_{SF} is the stacking fault width; and (*iii*) the work done by an external stress τ aiding in forming the stacking faults (Kibey et al., 2007; Galindo-Nava and Rivera-Díaz-del-Castillo, 2017): $E_\tau = \frac{\tau}{m_{SF}} b r^2 n$, where the area r^2 represents the area screened by a dissociating dislocation towards forming a stacking fault and $m_{SF} = 0.31$ is the Schmid Factor of a partial forming in the $\langle 112 \rangle \{111\}$ system. σ_{HCP}=11.5 mJ m^{-2} was found optimal for steels and this value is also considered for Ni-based superalloys to simplify the assumptions. It is worth noting that, to the authors knowledge, there are no experimental or theoretical values of σ_{HCP} in superalloys in published literature. Since the aim of this work is to have the lowest number of fitting parameters, it is considered that using the same value of σ_{HCP} as in austenitic steels – with similar ranges in the stacking fault energy – is an acceptable assumption.

It is assumed that the same energy balance holds for stacking fault formation leading to microtwinning in superalloys but in this case the nucleation takes place at the γ/γ' interface (Viswanathan et al., 2005; Fu et al., 2015). This is because the opposing force to form an anti-phase boundary is acting as stress concentrator in the γ/γ' interface (Karthikeyan et al., 2006). Such implies that the dissociating dislocations are subjected to additional stress, reducing the effective stress to form a twin. Another energy term is added to E_c to account for local stress concentrations (due to the γ') in a similar fashion as in Karthikeyan et al. (2006): $E_{APB} = \frac{\gamma_{APB}}{2b} f_{\gamma'} b r^2 n$, where $f_{\gamma'}$ is the γ' volume fraction; this equation represents the effective stress increase at the γ/γ' interface when the fraction of γ' increases. The critical energy can be expressed as:

$$E_c = E_{dis} + E_{nuc} - E_\tau - E_{APB}. \tag{1}$$

It is worth noting that the strain energy has been considered in the energy balance via E_{dis}, *i.e.* the energy to form a dislocation partial, as consequence of an applied stress (E_τ). A twin embryo forms when the critical strain energy is at a minimum ($\frac{\partial E_c}{\partial r} = 0$), leading the stacking fault width (r^*) to be:

$$\frac{n\mu b^2}{2\pi(1-\nu)}\left(\ln\left(\frac{r^*}{2bn^2}\right) + 1\right) + (\gamma_{SFE} - \sigma_{HCP})r^* l_{SF} - \left(\frac{\tau}{m_{SF}} + \frac{\gamma_{APB}}{2b} f_{\gamma'}\right)2br^* = 0. \tag{2}$$

This equation can be solved numerically to obtain r^* in terms of the stacking fault energy. It is assumed that r^* satisfies Eq. (2) when τ is maximum leading to a local minimum energy (see in Galindo-Nava and Rivera-Díaz-del-Castillo (2017) for further discussion and details on the solution method); this implies that τ represents the critical stress concentration at the γ/γ' and it is independent of the macroscopic applied stress, assuming it is high enough to promote slip. It is interesting to compare the values predicted for r^* against experimental results; the magnitude of the Burgers vector, shear modulus and Poisson's ratio are considered equal to those for pure nickel to simplify the calculations (Galindo-Nava et al., 2015): $b = 0.248$ nm, $\mu = 80$ GPa and $\nu = 0.31$. For instance, typical values of a disc alloy are $\gamma_{SFE} = 25$ mJ/m^2, $\gamma_{APB} = 0.3$ mJ/m^2 and $f_{\gamma'} = 45\%$, and the predicted critical width is ~ 3 nm; this value is consistent with experimental observations in several superalloys reporting the width of nano-twins and stacking faults being in the range 2–5 nm (Viswanathan et al., 2005; Xu et al., 2014; Smith et al., 2006). This shows that the model for twin nucleation in principle is applicable to superalloys, although more information on the twin structure is needed. Moreover, the resolved shear stress to cut a γ' precipitate using the same parameters as before is approximately $\frac{\gamma_{APB}}{2b} \sim 604$ MPa (Reed, 2006), whereas the local stress induced by the stacking fault of width r^* is $\frac{\gamma_{SFE} r^*}{2b^2} \sim 609$ MPa; this indicates that the critical resolved shear stress should meet at the γ/γ' interface once the critical stacking fault width is met.

Step 2: Force balance at the γ/γ' interface

Once a stacking fault nucleates, the onset of particle shear will occur when the force produced by a stacking fault equals to an opposing force by the anti-phase boundary preventing γ' cutting (Reed, 2006). The force balance can be defined in the same way as that for a dislocation pair cutting a γ' particle, *i.e.* the strong and weak pair coupling model (Galindo-Nava et al., 2015). The acting force on a single γ' can be approximated by the product of the shear stress induced by a stacking fault and the mean particle spacing (Reed, 2006): $\tau_{SF}(\Lambda_{\gamma'} - 2r)$; this configuration is analogous to the case of a "strong pair-coupling" dislocation (Galindo-Nava et al., 2015). τ_{SF} can be approximated by $\frac{2\gamma_{SFE}}{b}$ (Talonen and Hänninen, 2007). The opposing force equals to $2\gamma_{APB}r_{shear}$, where r_{shear} is the length of initial penetration by a stacking fault. This leads to the balance (Galindo-Nava et al., 2015):

$$\frac{2\gamma_{SFE}}{b}(\Lambda_{\gamma'} - 2r)b - 2\gamma_{APB}r_{shear} = 0. \tag{3}$$

In this case no force term due to the dissociation of a dislocation is included in the force balance; this is because it is assumed that the stacking fault has already formed and it will not convert back into a $\frac{1}{2}\langle 110 \rangle$ dislocation. Rearranging terms, r_{shear} becomes:

$$r_{shear} = \frac{\gamma_{SFE}(\Lambda_{\gamma'} - 2r)}{\gamma_{APB}}. \tag{4}$$

This parameters describes the ability of a stacking fault to cut a γ' particle and represents the cutting length of the SF once the critical stress is exceeded, in a similar fashion as the strong/weak pair coupling model (Reed, 2006).

Steps 3 and 4: Creep and stacking fault shear evolution

Dyson has proposed a mechanistic approach to describe creep controlled by dislocation climb in precipitation-hardened alloys (Dyson, 2009). The equation he derived is based on determining the frequency of dislocations encountering γ' precipitates and the variation in the dislocation density is dictated by the ability of dislocations to climb around impenetrable particles. The latter is proportional to the alloy's diffusion coefficient, as this process is assisted by vacancy diffusion. An equation to determine the evolution of the stacking fault density when γ'–shear is the rate-controlling mechanism can be postulated following similar arguments: The increase in stacking fault density (ρ_{SF}) is dictated by the encountering frequency of stacking faults with γ' particles; the shear process will slow down stacking fault propagation, hence the rate will be lower when increasing the number density of γ' particles or if the precipitates are difficult to shear. The former is captured by considering that the density of planar faults being in contact with γ' particles in a grain is $\rho_{SF} N'_{\gamma}$ where $N'_{\gamma} = \left(\frac{\Lambda_{\gamma'} - 2r}{D}\right)$ (Dyson, 2009), with $\Lambda_{\gamma'} = \left(\frac{\pi}{4 f_{\gamma'}}\right)^{1/2} 2r$ being the mean particle spacing in the cross-section of a grain and D is the mean grain size (Fig. 2d). N'_{γ} is the inverse number of γ' particles present in a given slip plane in a grain (Unocic et al., 2008; Reed, 2006) and $1/N_{\gamma'}$ represents the number of shear events before stacking faults reach the grain boundaries. This is schematically shown in Fig. 2(d), where the number of obstacles for stacking fault propagation increases if the grain size increases or the particle spacing decreases. This result indicates that superalloys with fine grain size will see higher primary creep strain rates as stacking faults can reach grain boundaries promptly promoting grain boundary-controlled failure; this is consistent with experimental reports on grain size effects in creep (Locq et al., 2004). In addition, experimental evidence -first proposed in the 1960s (Li, 1963)- (Bauer et al., 2012; Messe, 2015; Ram et al., 2016; Kienl et al., 2022; Monni, 2021) and modelling (Tschopp and McDowell, 2008) suggest grain boundaries can act as dislocation sources, either directly (along their length or at triple points) or indirectly, via grain boundary precipitates such as carbides and borides or serrations affecting local stress conditions. This then indicates that the increase in stacking fault density is inversely proportional to the grain size, as the previous equation suggests. In Dyson's model an additional term $\frac{b}{r_{\gamma'}}$ is included to estimate the effective fraction of dislocations being able to escape once a climb event has occurred, as they do not interact with all γ' particles. For the case of stacking fault shear, this term can be considered as the ratio between the distance of initial penetration of a stacking fault, r_{shear} (Eq. (4)), and the radius of a γ' particle to account for the fraction of a γ' particle involved in the initial shear process. The fraction of the stacking fault density in contact with a shearable particle is then equal to $\frac{\pi}{N_{\gamma'}} \frac{r_{shear}}{r_{\gamma'}} \rho_{SF}$. If it is assumed that stacking faults shear the γ' at a shear frequency Γ_{shear}, the evolution equation for the stacking fault density is given by Dyson (2009):

$$\frac{d\rho_{SF}}{dt} = \frac{\pi}{N_{\gamma'}} \frac{r_{shear}}{r_{\gamma'}} \Gamma_{shear} \rho_{SF}. \tag{5}$$

This equation gives the evolution of the stacking fault shear process during tertiary creep but does not provide information on primary creep (Dyson, 2009; Zhu et al., 2012; Yuan et al., 2012) and no effects of multimodal γ' distributions have been considered. We now include the latter. In addition, we note that dislocation evolution is considered in the model via Eq. (5), where it is implicitly assumed that the dislocation density increases as stacking fault shearing takes place, leading to additional dislocations that will also split into partials and form stacking faults.

Since experimental evidence and theoretical models indicate that the size of the tertiary γ' is typically smaller than the width of stacking fault, it is assumed that the tertiary γ' is sheared athermally by stacking faults (Karthikeyan et al., 2006; Unocic et al., 2008). This means that the stacking fault can easily shear the tertiary γ' precipitates and this process will only delay the main shearing processes taking place at the secondary γ'/γ interface. Such frequency will depend on the number of tertiary γ' particles the stacking fault will encounter between two secondary γ' particles, which can be estimated by the mean free path ratio (Fig. 2(e)):

$$N_{inter} = \frac{\Lambda_{ter}}{2(\Lambda_{sec} - 2r_{sec})} \tag{6}$$

with $\Lambda_{ter} = \frac{r_{ter}\pi}{f_{ter}^{1/2}}$ and $\Lambda_{sec} = \frac{r_{sec}\pi}{f_{sec}^{1/2}}$ where tertiary γ' particles are considered as point obstacles. This equation indicates that if the tertiary γ' spacing is equal to the secondary γ' one, *i.e.* $N_{inter} = 1/2$, then tertiary γ'-free regions -where stacking fault propagation is easy- are split into two and the same number of stacking fault shear events take place; conversely, if there are several tertiary γ' precipitates, *i.e.* Λ_{ter} is small, then the number of tertiary γ' shear events increases with N_{inter} making the arrival of a stacking fault to the secondary γ' much more slow. In order to capture the delaying effect and the fact that the volume fraction of tertiary γ' can be zero, we use an harmonic equation between the case when there is no tertiary γ' ($N_{inter} = 1$) and when tertiary γ' is present:

$$N^*_{ter} = \frac{1}{1 + \frac{1}{N_{inter}}} = \frac{\Lambda_{ter}}{2(\Lambda_{sec} - 2r_{sec}) + \Lambda_{ter}} \tag{7}$$

From a phenomenological point of view, primary creep is generally induced by the initiation of stacking fault shearing (Rae and Reed, 2007). This indicates that the initial condition when solving Eq. (5) also depends on the extent of γ' shearing, *i.e.* the primary creep strain is proportional to the ratio $\frac{\Lambda_{sec} - 2r}{b}$ dictating the extent of stacking fault shear. This is consistent with experimental reports in Nimonic 263 where both primary and tertiary creep increase with increasing the γ' size (Angella et al., 2014). Solving Eq. (5), it gives the evolution of ρ_{SF} to be:

$$\rho_{SF} = \rho_0 \left(\frac{\Lambda_{sec} - 2r}{b}\right) \exp\left(\frac{\pi N^*_{ter}}{N_{sec}} \frac{r_{shear}}{r_{sec}} \Gamma_{shear} t\right) N^*_{ter}, \tag{8}$$

where ρ_0 is the initial dislocation density and the only missing parameter is Γ_{shear}. We note that $\Lambda_{\gamma'}$ in Eq. (5) considers the average γ' spacing for a monomodal particle size distribution, whereas in Eq. (8), $\Lambda_{\gamma'}$ is replaced by Λ_{sec} as shearing the secondary γ' is the main creep rate-controlling mechanism. It is worth noting that grain size effects are only considered in the equation for stacking fault density, via $N_{\gamma'}$, and other possible effects in creep, like the change in (perfect) dislocation density (as consequence of grain-boundary emission) affecting the primary and secondary creep rates are not included in the model. This issue is addressed in the Discussion and Results sections.

For a vacancy-induced climb event, the frequency of dislocation climb is proportional the vacancy mobility (diffusion coefficient) in the area covered by a single vacancy, b^2 (Friedel, 1964). Analogous to this, the frequency of stacking fault shearing is taken proportional to their mobility in the γ' and the proportionality constant is the area of a single stacking fault unit $r^* l_{SF}$, as schematically shown in Fig. 2(b). This gives the frequency to be (Dyson, 2009):

$$\Gamma_{shear} = \frac{1}{r^* l_{SF}} M_{SF}. \tag{9}$$

Kolbe (2001) has suggested that the mobility of stacking faults in the γ', M_{SF}, is thermally activated and it should have the form $M_{SF} = M_0 \exp\left(-\frac{E_{shear} - V_{SF}\tau}{RT}\right)$ m^2/s, where E_{shear} and V_{SF} are the activation energy and volume involved during stacking fault propagation in the γ', respectively. In addition, this process should include short range diffusion of Co and Cr in the γ', and M_{SF} should be proportional to the effective diffusion coefficient of Co and Cr segregating to the stacking faults (Kovarik et al., 2009): $M_{SF} \propto D_{SF}$, where D_{SF} is the effective diffusion coefficient of Co and Cr in the γ'. Additionally, the formation of a super extrinsic stacking fault requires local energy increase to form two adjacent Shockley partials and a complex stacking fault in the γ' (Karthikeyan et al., 2006); thus, the energy penalty for stacking fault propagation should correspond to the energy of forming these partials and E_{shear} can be approximated by the stacking fault energy screened on each partial (Friedel, 1964): $E_{shear} = (2\gamma_{SP} d_{SP} b + \gamma_{CSF} d_{CSF} b) N_a$, where N_a is the Avogadro's constant. In practice, it is difficult to measure the stacking fault energies in the γ', but the stacking fault energy of the respective partial can be estimated from the mean partial spacing by Yuan et al. (2011a): $\gamma_i = \frac{(2+\nu)\mu b^2}{8\pi(1-\nu)d_i}$. This leads the activation energy to be:

$$E_{shear} = \frac{3(2+\nu)\mu b^3}{8\pi(1-\nu)} N_a. \tag{10}$$

The stacking fault mobility then equals to:

$$M_{SF} = D_{SF} M_0 \exp\left(-\frac{E_{shear} - V_{SF}\tau}{RT}\right) \text{ [m}^2 \text{ s}^{-1}], \tag{11}$$

where M_0 was fitted to 3×10^{14} for all alloys tested. $V_{SF} = 3.3\times10^{-4}$ m^3/mol was adjusted for all alloys tested. This value is consistent with Manonukul et al. (2002), where they fit a creep activation volume of 2.9×10^{-4} m^3/mol in C263 at higher temperatures and low stress levels.

The creep strain ε in superalloys consists of the strain accommodated by $\frac{1}{2}\langle 110 \rangle$ dislocations (ε_{dis}) and by stacking faults propagating in the γ and γ' (ε_{SF}):

$$\varepsilon = \varepsilon_{dis}(1 - f_{SF}) + \varepsilon_{SF} f_{SF} \tag{12}$$

where f_{SF} is the relative fraction of stacking fault activity with respect to dislocation propagation. The first term is relevant at temperatures in excess of 750 °C and low applied stress levels, where diffusion-controlled climb around the γ' is promoted (Smith et al., 2006), hence it will be assumed that stacking fault shear fully controls the creep strain for $T \leq 750$ °C, i.e. $\varepsilon \approx \varepsilon_{SF}$ and $f_{SF} \approx 1$ (Viswanathan et al., 2005). ε_{SF} is linked to the stacking fault density by employing the Orowan equation:

$$\varepsilon_{SF} = b \rho_{SF} \Delta L_{SF}, \tag{13}$$

where ΔL_{SF} is the stacking fault shear distance. In order to describe the dislocation slip distance during creep of low stacking fault energy alloys, Friedel proposed a combined mechanism of jog-diffusion and cross-slip (Friedel, 1977); the former is responsible for triggering dislocation slip and the latter controls the energy penalty for dislocations to continue gliding. This process has been captured for Ni-based alloys in previous work by using a parabolic law for the dislocation glide distance (Galindo-Nava and Rae, 2016), where this law accounts for jog–diffusion and the activation energy includes that for cross-slip. This mechanism is very similar to the process required for stacking faults to shear in the γ', where both diffusion and stacking fault formation are involved. The equation for ΔL_{SF} has been validated against experimental data for Cu, Ni, Ti and 4 Ni-base alloys, via predicting primary and secondary creep, under a wide range of conditions in temperature, applied stress and initial microstructure. This gives us the confidence that dislocation creep in Ni-based superalloys can be described using the same mathematical formalism. It will then be assumed that ΔL_{SF} follows a parabolic law with M_{SF} in Eq. (11) as the effective mobility of the stacking faults:

$$\Delta L_{SF} = \sqrt{M_{SF} t}. \tag{14}$$

This equation indicates that short-range diffusion is necessary to trigger stacking fault propagation, whereas M_{SF} captures the high energy penalties involved in the reordering and additional stacking fault formation. No effects of the stacking fault mobility in the γ are considered in ΔL_{SF} or in ε, since the energy required for stacking fault propagation in the γ' is much greater than in the disordered γ, hence the former is the rate-controlling factor (Section 4.1). This is consistent with experimental reports concluding that the contribution of dislocation glide in the γ to the creep strain is negligible in single-crystal superalloys (Rae and Reed, 2007). The evolution of creep deformation is obtained by combining Eqs. (8) and (13).

Table 3

Coefficients for γ_{SFE} and γ_{APB} estimations.

Element	Co	Cr	Mo	W	Fe	Al	Ti	Nb	Ta
α_i (mJ/m^2)	4.67	8.99	21.15	19.74	5.85	6.11	14.4	20.4	18.2
β_j (mJ/m^2)	–	−1.4	−1.4	3.7	–	–	12	17.12	21.7

Table 4

γ composition (in at%) of the superalloys tested.

Alloy	Ni	Co	Cr	Mo	W	Fe	Al	Ti	Nb	Ta	Ref.
RR1000	Bal.	25	28	4.8	–	–	1.5	0.001	–	–	Jones et al. (2014)
AllVac718plus	Bal.	11	26	2	0.4	11	0.6	0.1	–	–	Viskari and Stiller (2011)
NiSup1	Bal.	7.1	26	2.9	0.6	–	0.9	0.6	–	–	Tian et al. (2014)
NiSup2	Bal.	20	25	2.9	0.6	–	0.87	0.6	–	–	Tian et al. (2014)
NiSup3	Bal.	31	25	2.9	0.6	–	0.8	0.6	–	–	Tian et al. (2014)
Udimet 720Li	Bal.	20	26	3	0.5	–	1.2	0.3	–	–	Yuan et al. (2011a)
René 88DT	Bal.	15	23	5	2	–	1.6	0.5	–	–	Hwang et al. (2009b)
ME3	Bal.	30	23	4	1	–	4.9	2	0.4	0.4	Olson et al. (2008)
TMW-4M3	Bal.	34	27.1	2.5	0.5	–	0.9	0.4	–	–	Yuan et al. (2011a)
TMW-2	Bal.	29.8	27.4	2.6	0.6	–	0.9	0.4	–	–	Yuan et al. (2011a)
MC2	Bal.	9.1	25.9	2.75	4.1	–	2.9	0.3	–	–	Benyoucef et al. (1995)

4. Results and discussion

4.1. Estimating model parameters

The stacking fault energy in the γ and the anti-phase boundary energy of the γ' are critical components in the model for creep and proper estimation of these parameters with varying composition is required. A number of atomistic approaches have been proposed to calculate the stacking fault and antiphase boundary energies with chemical composition (Mishin, 2004; Vamsi and Karthikeyan, 2012; Crudden et al., 2014; Shang et al., 2012; Chandra and Sondhi, 2011). For the case of the stacking fault energy in FCC Ni-alloys (γ), Shang et al. (2012) have found that γ_{SFE} can be described by a linear combination of the alloying concentrations in the γ (x_i^γ) as:

$$\gamma_{SFE} = \gamma_{SFE}^{Ni} - \sum_i \alpha_i x_i^\gamma, \tag{15}$$

where the α_i coefficients are obtained from DFT calculations and γ_{SFE}^{Ni} is the stacking fault energy of pure Ni, whose values have been reported to lie in the range 100–200 mJ/m^2 (Humphreys and Hatherly, 2004; Shang et al., 2012; Chandra and Sondhi, 2011); $\gamma_{SFE}^{Ni} = 100$ mJ/m^{-2} was adopted in the present calculations. Similarly, Crudden et al. (2014) have shown that the variation in the antiphase boundary energy with alloying can be expressed as a linear combination of the solute concentrations in the γ' ($x_j^{\gamma'}$):

$$\gamma_{APB} = \gamma_{APB}^{Ni_3Al} + \sum_j \beta_j x_j^{\gamma'}, \tag{16}$$

where $\gamma_{APB}^{Ni_3Al} = 195$ mJ/m^2 is the antiphase boundary energy of Ni$_3$Al (Crudden et al., 2014). The values of α_i and β_j reported by Shang et al. and Crudden et al. reproduce the trends well when modifying the chemical composition, however in practice, the predicted values are higher than the experimental measurements. For instance, the reported slope change with Co additions (α_{Co}) is ≈ 4.6 mJ/m^2, however experimental estimations in Zhi'an et al. (1988) and Yuan et al. (2011a) suggest that $\alpha_{Co} \sim 0.6 - 1$ mJ/m^2. Similarly for γ_{APB}, the predicted yield strength in Crudden et al. (2014) using Eq. (16) ($\sigma_Y \propto \gamma_{APB}$) was higher than the measured strength in most of the alloys under consideration. Therefore, it is necessary to introduce corrections in the coefficients of Eqs. (15) and (16) in order to calculate the fault energies in multicomponent alloys. Correction factors of 0.165 for α_i and 0.8 for β_j were found optimal for the alloys tested and Table 3 shows the values reported in Shang et al. (2012) and Crudden et al. (2014) for the alloying elements considered in this work (including the corrections). Fig. 3 shows a comparison between the predicted and measured the stacking fault energies in several superalloys. The experimental stacking fault energy is calculated by measuring the equilibrium partial dislocation separation d_{sep}, requiring high-resolution TEM, and fitting γ_{SFE} to an equation of the form (Pierce et al., 2014): $\gamma_{SFE} \propto \frac{\mu b^2}{d_{sep}}$, where the proportionality constant depends on the dislocation character angle. The γ composition to perform the calculations is shown in Table 4. The predictions show good agreement for the compositional range under consideration, showing that γ_{SFE} is indeed very sensitive to variations in the γ composition (Table 1). As for the antiphase boundary energy, the predicted values in RR1000, René88DT, Udimet 720Li and ME3 are 337, 316, 338 and 334 mJ/m^2, respectively, with these values being in the same range as the predicted values using CALPHAD and DFT calculations (Crudden et al., 2014). These results allow us to apply the creep model to alloys where no reports on the fault energies are available by only using the chemical composition in the γ and γ'.
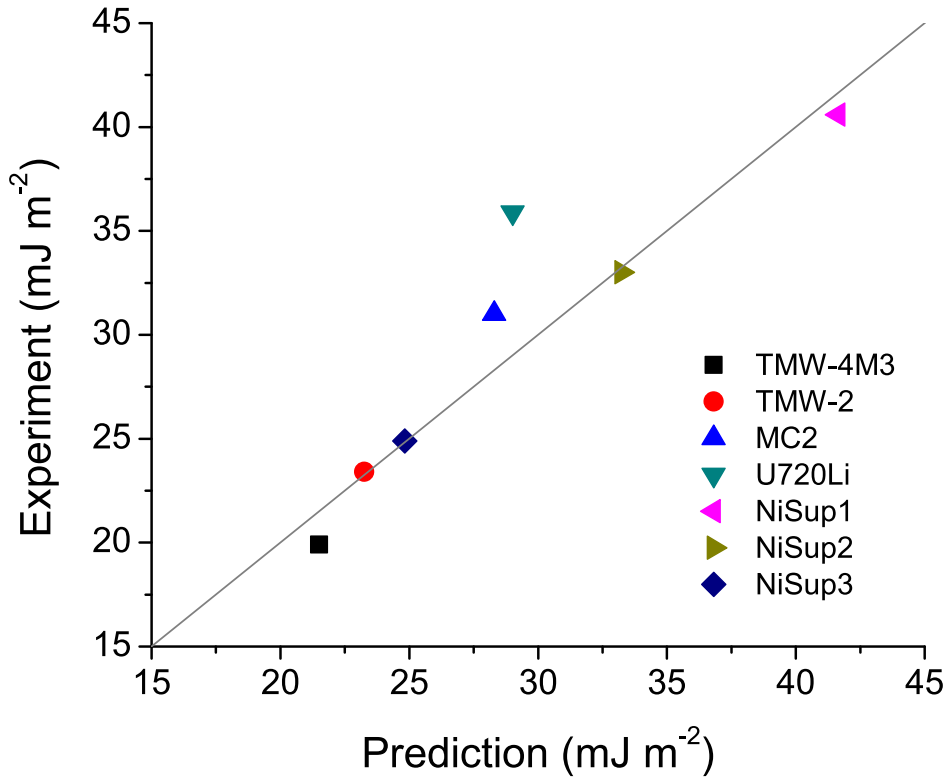
Fig. 3. Predicted *vs* measured stacking fault energy using a linear approximation.

The effective diffusion coefficient of Co and Cr segregating to the γ' can be estimated with the harmonic relation (Zhu et al., 2012):

$$D_{SF} = \cfrac{1}{\cfrac{x_{Co}^{\gamma'}}{(x_{Co}^{\gamma'}+x_{Cr}^{\gamma'})D_{Co}^{\gamma'}} + \cfrac{x_{Cr}^{\gamma'}}{(x_{Co}^{\gamma'}+x_{Cr}^{\gamma'})D_{Cr}^{\gamma'}}}, \tag{17}$$

where $x_{Co}^{\gamma'}$ and $x_{Cr}^{\gamma'}$ are the concentrations of Co and Cr in the γ'; $D_{Co}^{\gamma'} = D_{Co,0}^{\gamma'} \exp\left(-\frac{Q_{Co,\gamma'}}{RT}\right)$ and $D_{Cr}^{\gamma'} = D_{Cr,0}^{\gamma'} \exp\left(-\frac{Q_{Cr,\gamma'}}{RT}\right)$ are the diffusion coefficients of Co and Cr in the γ', respectively. The diffusion parameters have been obtained from the literature (Cermak et al., 2003): $D_{Co,0}^{\gamma'} = 3 \times 10^{-3}$ m^2/s and $Q_{Co,\gamma'} = 304$ kJ/mol for Co and $D_{Cr,0}^{\gamma'} = 6.8 \times 10^{-4}$ m^2/s and $Q_{Cr,\gamma'} = 303.4$ kJ/mol for Cr.

4.2. Experimental results

Fig. 4(a) shows the creep test results in RR1000 for the typical (red dots) and fine (blue dots) microstructures. High stress creep testing revealed that the fine microstructure deforms with lower creep rates at 900 MPa compared to the typical microstructure. Meanwhile, the equivalent relative stress level of 90% yield stress at 800 MPa in the typical microstructure led to the lowest creep rates. The fine microstructure suffered from a significant ductility loss, as reported for other fine precipitate microstructures (Collins and Stone, 2014; Xia et al., 2007; Chang and Liu, 2001), with the failure originating in the sample thread. A repeated test yielded the same early failure within the thread.

The typical microstructure sample tests were interrupted before they reached entirely constant creep rates but both approached this regime; the minimum creep rate measured at 900 MPa being 1.53×10^{-6} s^{-1} and at 800 MPa being 1.49×10^{-7} s^{-1}; the fine microstructure sample failed well within the primary creep regime with a minimum creep rate of 1.06×10^{-6} s^{-1}.

4.3. Model results

The model predictions are tested against experimental measurements in several superalloys (Table 1). This is done by solving Eqs. (8) and (13), where the input parameters are deformation conditions (T and σ), γ and γ' composition, grain size and initial γ' structure. A low initial dislocation density $\rho_0 = 10^{11}$ m^{-2} is considered in all cases; this value is consistent with previous work on creep in Ni (Galindo-Nava and Rae, 2016). A Taylor orientation factor $M = 3$ is considered in polycrystalline superalloys to transform the applied axial stress to shear stress $\tau = \frac{1}{M}\sigma$ (Galindo-Nava et al., 2015). MATLAB scripts with the solution of the models are
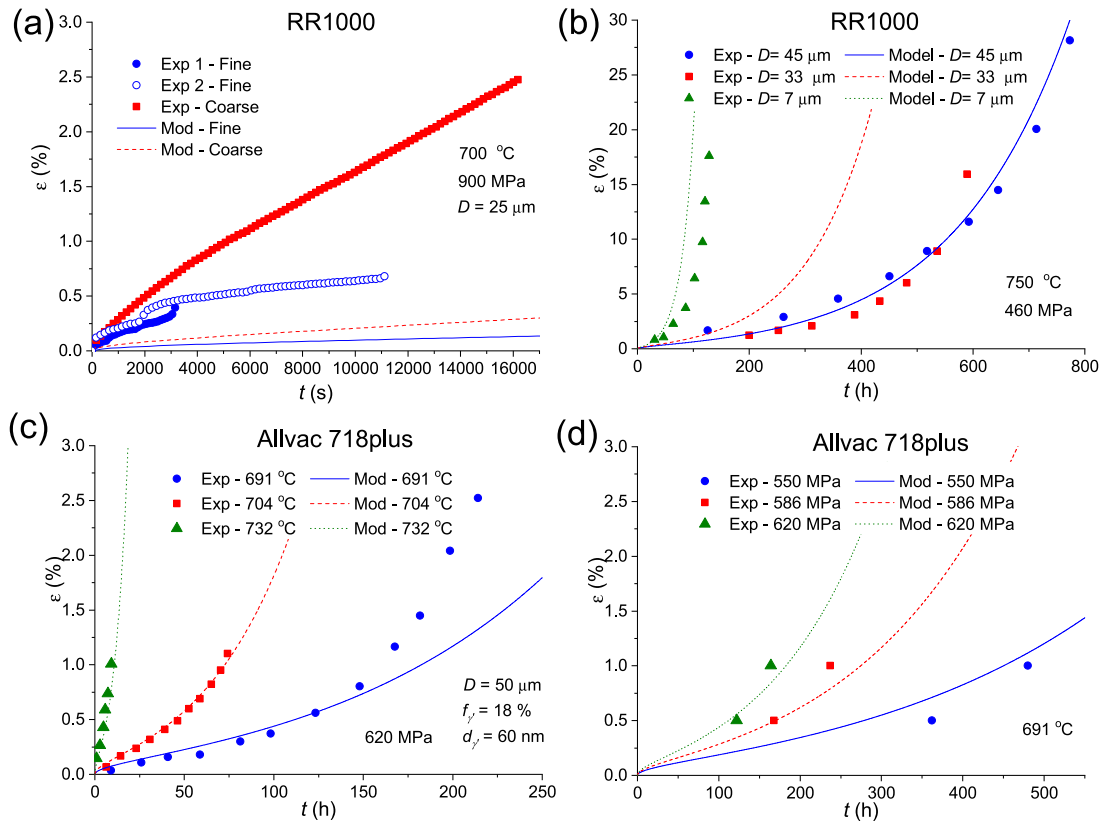
Fig. 4. Model predictions and experimental validation in RR1000 with (a) different γ' structure and (b) grain size. Additional results in Allvac 718Plus at different (c) temperatures and (d) stress levels. (For interpretation of the references to colour in this figure legend, the reader is referred to the web version of this article.)

included as supplementary material. Effects of the initial microstructure, deformation conditions and stacking fault energy are tested in this section. Chemical composition effects are explored in Section 4.4.

Fig. 4(a) shows a comparison between the model predictions and measurements in RR1000 with two initial microstructures. The model predicts lower primary creep in both cases, although the sensitivity of the primary creep with microstructure is well reproduced by the model; this indicates that an alloy with fine (almost monomodal) γ' distribution has better creep response than its coarse variant, although its ductility is severely reduced (Collins and Stone, 2014). Moreover, it is observed and predicted that the primary creep strain in the alloy with typical microstructure is higher, in spite of having finely dispersed (30 nm) tertiary γ'; this is due to the coarser secondary γ' producing a higher stacking fault density when sheared. This confirms that the effects of the γ' structure in Eq. (8), via $N_{\gamma'}$ and the primary creep factor are well reproduced. Possible reasons for model mismatch in Fig. 4(a) could be additional grain size effects not considered in the model, such as enhanced dislocation emission/pile-up at grain boundaries promoting primary creep strain (ε_{dis} in Eq. (12)), as the model captures well the tertiary creep behaviour in figure (b), where stacking fault shear should already dominate the process. Expressions for ε_{dis}, *e.g.* describing dislocation recovery could be explored in future work. Another key microstructural feature involved in creep deformation is the grain size; Fig. 4(b) shows the model predictions and experimental validation in RR1000 with different initial grain size and similar γ' structures. The experimental data were obtained from Connor (2009) and detailed information on the γ' structure can be obtained in Galindo-Nava et al. (2015). The grain size ranges between 7 µm and 45 µm and the deformation conditions are $T = 750\ °C$ and $\sigma = 460$ MPa. The model shows good agreement when $D = 7$ and 45 µm, however there is significant variation in the experiments when the grain size is 33 µm; a reason for this can be due to possible heterogeneities in the microstructure, as the tests were done in different locations of a gas turbine disc undergoing a dual-microstructure heat treatment (Connor, 2009), and local variations in the thermal gradient could modify the local microstructure; more results will be shown in other alloys with different grain sizes. It is also interesting to note that, when comparing the experimental results, grain size variations affect greatly tertiary creep but do not produce any significant effect during primary creep; the model is consistent with this phenomenon, by considering that D affects the extent of stacking fault propagation during tertiary creep (Eq. (8)). In order to explore the effects of deformation temperature and applied stress, Fig. 4(c) and(d) show the predictions and experimental results in Allvac 718plus. The data were obtained from Hayes et al. (2015) and this alloy has only secondary γ' (unimodal size distribution) with mean size 60 nm and volume fraction of 18% (Hayes et al., 2015); only
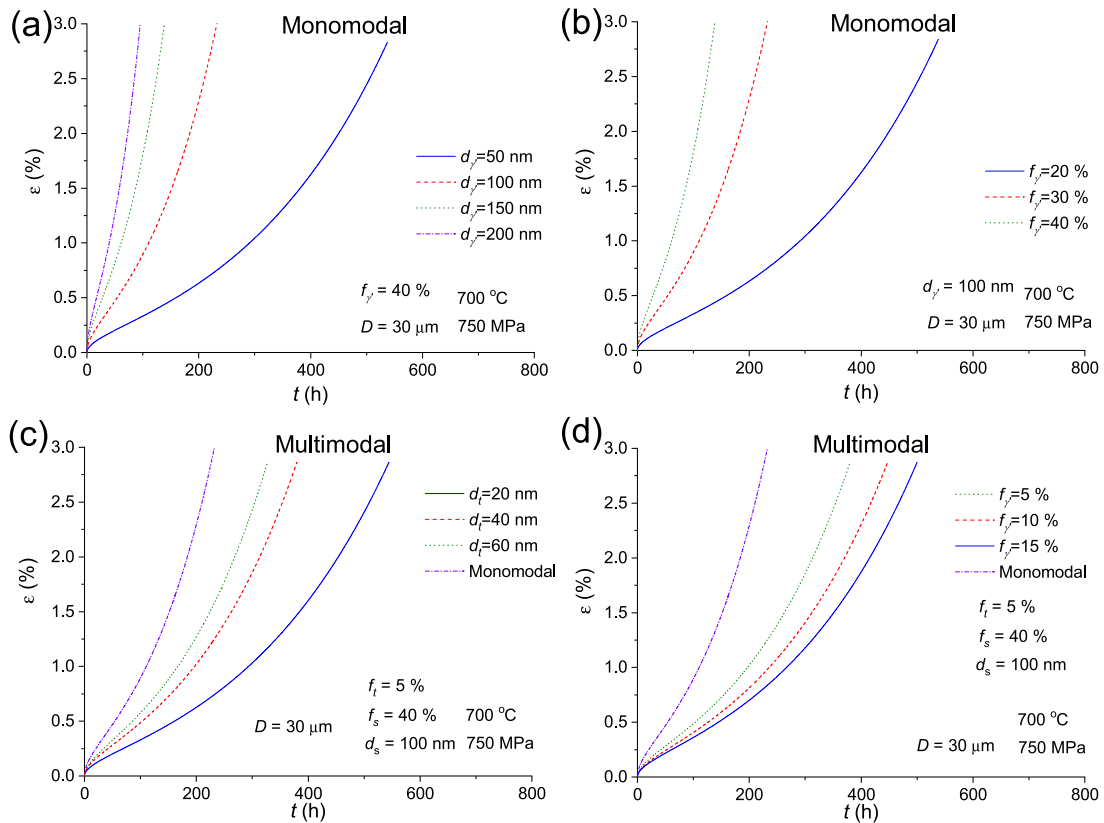
Fig. 5. Predicted γ' effects in RR1000 holding a monomodal γ' structure with different (a) sizes and (b) volume fraction. Results in RR1000 with multimodal particle size distribution and different tertiary γ' (a) size and (b) volume fraction. (For interpretation of the references to colour in this figure legend, the reader is referred to the web version of this article.)

γ' shear is operating as opposed to dislocation climb or Orowan looping.[1] The model shows very good agreement with experiments in all cases; these results show that γ' shear strongly depends on the testing temperature, as the time to reach 1% strain at 620 MPa decreases from ~150 h at 691 °C to ~10 h if the temperature only increases by 41 °C (732 °C); the model predicts this effect confirming that the activation energy in M_{SF} in Eqs. (8) and (14) is controlled by atom reordering and superlattice stacking fault formation.

It is possible to assess the effects of the γ' structure in the creep response using the model. We take RR1000 deformed at 700 °C and 750 MPa with $D = 30$ µm as a reference case. Fig. 5(a) and (b) show the predicted creep strain response in a monomodal alloy with different secondary γ' size and volume fraction, respectively; specific secondary γ' structures can be achieved by controlling the cooling rate from the solution heat treatment step followed by subsequent ageing (Section 3). The creep resistance increases significantly when decreasing the γ' size; for instance, the difference between the time to reach 3% strain between $d_{\gamma'} = 50$ nm and $d_{\gamma'} = 200$ nm is ~ 500 h, indicating that fine γ' microstructures improve the creep life. Similarly in Fig. 5(b), increasing the γ' volume fraction has a positive effect in the creep resistance of the alloy; if $f_{\gamma'}$ increases from 20% to 40%, the time to reach 3% creep strain increases by ~ 500 h. This analysis confirms that the microstructure has a strong influence in creep deformation. Additionally, the model results are explored in RR1000 holding multimodal γ' size distributions, as these structures are optimal for improving other mechanical properties (Galindo-Nava et al., 2015). Fig. 5(c) and (d) show the predicted creep strain response when the structure of the secondary γ' is fixed and the (c) size and (d) volume fraction of the tertiary γ' changes, respectively; an additional calculation for microstructures with no tertiary γ' (purple line) is included in the figures to compare the effects between monomodal and multimodal γ' size distributions. Controlling the size and fraction of the tertiary γ' is possible by tailoring specific ageing steps (Jackson and Reed, 1999). Similar to the previous case, the creep strength improves when the size of the tertiary γ' decreases or its volume fraction increases; this is due to the higher number density of particles present in the alloy reducing the extent of stacking fault shear, via N_{ter}^*. Moreover, when comparing Fig. 5(a), (c) and (d) similar response is predicted in alloys having a monomodal γ' distribution with $d_{\gamma'} = 50$ nm and 40% (blue line in (a)) or multimodal size distributions with $d_s = 100$ nm, $f_s = 40\%$, $d_t = 20$ nm and $f_t = 5\%$ (blue line in (c)) or $d_s = 100$ nm, $f_s = 40\%$, $d_t = 40$ nm and $f_t = 10\%$ (red line in (d)). These results

---

[1] In the figure $d_{\gamma'}$ and $f_{\gamma'}$ denote the size and volume fraction of secondary γ', respectively.
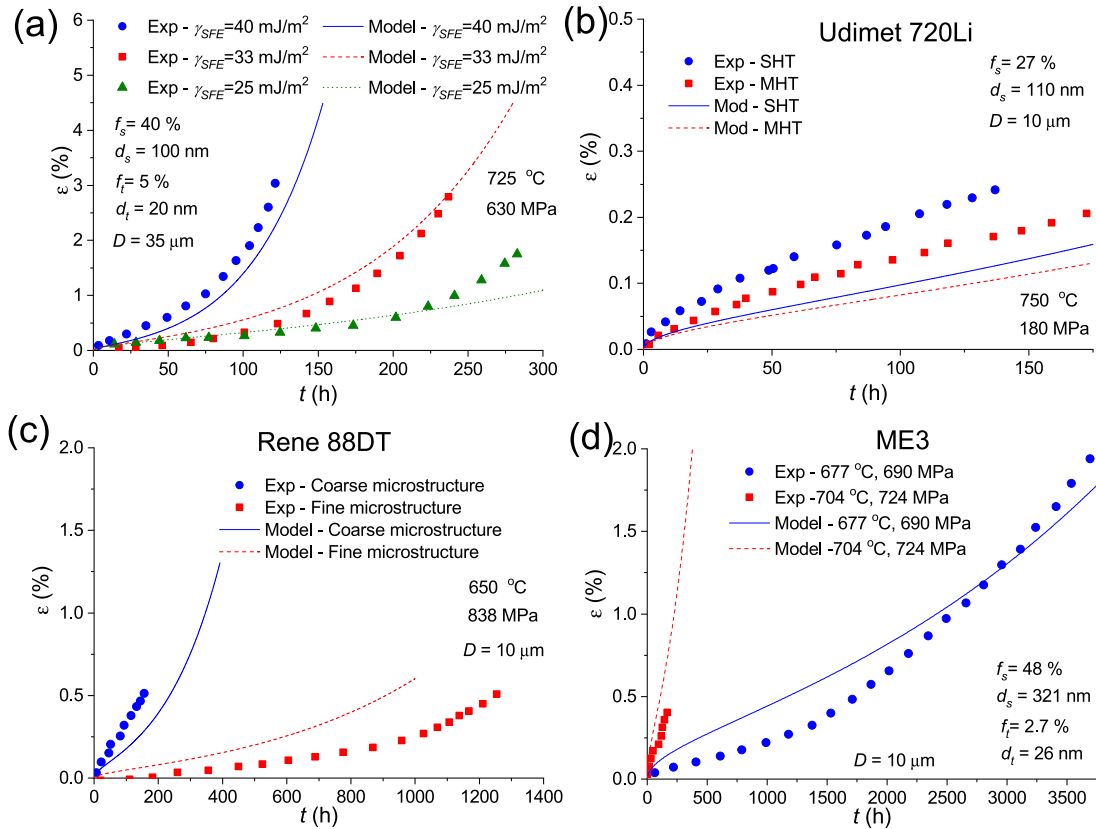
Fig. 6. (a) Stacking fault energy and (b) microstructure effects in the creep response in Udimet 720Li. Model predictions and experimental validation of creep deformation in (c) René 88DT and (d) ME3.

show that different microstructures can produce the same creep response. This is a useful result when designing γ' structures for other mechanical properties whilst targeting at a specific creep life.

Fig. 6 shows results exploring combined effects of the stacking fault energy and microstructure. Fig. 6(a) depicts the model predictions and experimental results in Udimet 720Li, NiSup1 and NiSup3; the last two alloys are derivatives of Udimet 720Li but with different Co content (Tian et al., 2014). These alloys have the same microstructure and γ_{SFE} is the only changing parameter (Table 2). The model shows good agreement for the two alloys with higher stacking fault energy, however lower creep strain is predicted in the alloy with the lowest γ_{SFE} values. This can be due to additional dislocation-stacking fault hardening interactions not being currently accounted for in the model. Results in Udimet 720Li with different microstructures are also shown in Fig. 6(b); the experimental data for creep at 750 °C and 180 MPa were obtained from Jackson and Reed (1999). Two microstructures are tested, in SHT condition the tertiary γ' structure is $d_t = 60$ nm and $f_t = 3\%$, whereas for the MHT $d_t = 42$ nm and $f_t = 3\%$; the secondary γ' structure is approximately fixed. The model shows very good results for the case of MHT, however it predicts lower primary and secondary creep; this can be due to additional stacking fault interactions and other diffusion-controlled effects that have not been introduced by the model, such as dislocation climb. These results show that the model is composition-sensitive, via the stacking fault energy, and microstructure-sensitive, via the tertiary γ', in the same alloy (Udimet 720Li) confirming that Eq. (8) captures well γ_{SFE} effects. To further support this, additional results in René 88 DT and ME3 are shown in Fig. 6(c) and (d), respectively. The former contains small additions of Nb (0.7 wt%) and high Mo+W content (8 wt%), whereas the latter includes additions of Ta (2.4 wt%) and Nb (0.9 wt%) but lower Mo+W content; these variations have important effects in the chemistry of the γ (Table 4) and γ' (Table 5). The model predictions in Fig. 6(c) are compared with experimental data obtained from Viswanathan et al. (2005) with two different microstructures; the Coarse microstructure consists of: $d_s = 200$ nm, $f_s = 35\%$, $d_t = 18$ nm and $f_t = 2\%$, whereas the Fine microstructure is formed by $d_s = 75$ nm, $f_s = 32\%$, $d_t = 14$ nm and $f_t = 14\%$; the largest difference between the two conditions is the finer secondary γ' and the higher tertiary γ' fraction in the Fine microstructure. The model shows reasonably good agreement against experiments, given the low strain values, highlighting that there is significant improvement in the creep strength if a fine microstructure is present in this alloy: the time to reach 0.5% creep strain is ≥ 1000 h in the Fine microstructure case, whereas it takes only ~ 200 h to reach the same strain level in the Coarse microstructure. Fig. 6(d) shows the results for ME3 deformed at different temperatures; the data were obtained from Smith et al. (2006).

The results shown that the model is able to reproduce creep deformation in various alloys with wide range in chemical compositions. For instance AllVac 718plus is rich in Nb, whereas René 88DT contains high Mo and W additions and RR1000 and

Table 5
γ' composition (in at%) of the superalloys tested.

Alloy	Ni	Co	Cr	Mo	W	Fe	Al	Ti	Nb	Ta	Ref.
RR1000	Bal.	6.6	1.2	0.7	–	–	12.5	9.5	–	1.4	Jones et al. (2014), Bagot et al. (2017)
Allv718plus	Bal.	3.5	0.8	–	–	1.3	11	3	8.9	–	Viskari and Stiller (2011)
NiSup1	Bal.	2.9	2.8	–	–	–	11	12	–	–	Tian et al. (2014)
NiSup2	Bal.	9.4	3.2	–	–	–	11	12	–	–	Tian et al. (2014)
NiSup3	Bal.	15.7	3.6	–	–	–	11	12	–	–	Tian et al. (2014)
Udimet 720Li	Bal.	9.4	3.2	–	–	–	11	12	–	–	Yuan et al. (2011a)
René 88DT	Bal.	7	2	2.5	1.6	–	12	9	0.8	–	Hwang et al. (2009b,a)
ME3	Bal.	12	2	2	0.42	–	12.8	8.2	1	1.2	Olson et al. (2008)

M3E also have Ta as alloying addition for γ' reinforcement. However, in most cases their microstructures were different, therefore a direct comparison of their creep performance is not straightforward using only the previous results. A parameter analysis is presented next to study individual alloy contribution whilst keeping the microstructure constant.

4.4. Parameter analysis: Chemical composition effects

One of the main novelties of the present approach is the introduction of chemistry effects in superalloys' creep response and it is possible to rank the creep strength of different alloys using the model. Fig. 7(a) shows the predicted creep strain in Udimet 720Li, RR1000, René 88DT and ME3 at 700 °C and applied stress of 725 MPa considering the same microstructure in all cases. It is predicted that RR1000 has the best creep performance, followed by ME3, René 88DT, whilst Udimet 720Li has the shortest creep life. These trends are consistent with the values of the stacking fault energy shown in Table 2, *i.e.* better creep life is achieved with lower γ–stacking fault energy.

It is also possible to assess the individual contributions of relevant alloying elements in commercial alloys to their creep life: Mo, W (γ partitioning) and Ti, Nb and Ta (γ' partitioning); Co effects are not considered since this has already been explored in Fig. 6(a). The γ and γ' composition of RR1000 (Tables 4 and 5) is considered for the remaining alloying elements, *i.e.* Ni-18.5Co-15Cr-Mo-W-3Al-Ti-Nb-Ta (wt%). Fig. 7(b) shows the creep strain predictions when Mo and W are absent in the γ (blue line), 5 Mo at% is added to the matrix (red line) and 5 W at% is present in the γ (green line). The increase in the creep strength is significant when Mo or W are added, with the time to reach 3% creep strain increasing by ~ 250 h; this is due to their strong effect in reducing the stacking fault energy in the γ (Table 2). It is also interesting to note that Mo and W produce similar effects, although Mo has a slightly stronger effect, since their contributions to the stacking fault energy are very similar (Table 3). Fig. 7(c) shows the predicted creep strain if Ti, Nb and Ta are removed from the γ' (blue line) and if 5% of Ti (red line), 5% of Nb (green line) or 5% of Ta (purple line) are introduced to the γ'; the γ' composition in all cases is Ni-25%(Al+Ti+Nb+Ta). In this case, it is also predicted that the creep strain is lower when Ti, Nb or Ta are present, with the latter having the strongest effect in creep, however the predicted strengthening is less significant than for γ partitioning elements. This is due to the γ_{SFE} driving stacking fault formation and subsequent shearing has a stronger effect in the creep rate, whereas γ' forming elements affect mainly the initial shear resistance, via γ_{APB} in Eq. (4). This is validated for the case of Co additions where the creep response was found to be highly sensitive to its variations, whilst the microstructure remained practically constant (Yuan et al., 2012).

From an alloy design perspective, tailoring the chemistry of the γ' is one of the main factors towards improving the tensile strength and the ratios Ti/Nb and Ti/Ta are the most significant rates to optimise. Fig. 7(d) shows the predicted time to reach 1% strain in RR1000 when varying the Ti content in the γ' from 0 up to 12 at.% and no Nb or Ta additions (blue line), and when substituting Ti for Nb (red line) or Ta (green line) and fixing Ti+Ta or Ti+Nb content to 12 at.%. It is interesting to note that the slope in the time to reach 1% creep strain changes when Ti≈ 8.5 at%, this is due to γ_{APB} affecting the rate of primary and tertiary creep; high primary creep is expected after short time if γ_{APB} is low, as r_{shear} is high, whereas if it increases, the extent of primary creep decreases and tertiary creep has greater effect in the strain increments. Additionally, it is confirmed that Ta has the strongest effect, due to its greater influence when increasing the anti-phase boundary energy; for instance, if the time to 1% strain is fixed to ~ 200 h, the combination 8%Ta+4%Ti has the same strengthening effect than the combination 12%Nb+0%Ti, or $> 12\%$ of Ti is required to reach the same strengthening levels. These results show that the model in principle can be used as a tool for designing alloys for creep resistance.

5. Discussion and concluding remarks

A model for creep at intermediate temperatures, between 650 °C and 750 °C, in Ni-based superalloys has been presented. The model is based on prescribing stacking fault nucleation, propagation and subsequent shear within the γ matrix and γ' precipitates. The stacking fault nucleation rate was derived from the critical formation energy, which depends on the γ–stacking fault energy (γ_{SFE}), anti-phase boundary energy γ' and γ' volume fraction. The equation was based on a previously introduced description for the twinning-induced plasticity effect in austenitic steels (Galindo-Nava and Rivera-Díaz-del-Castillo, 2017) but the strengthening effects of the γ' are added in the present case. The critical width to form a stacking fault embryo was compared against experiments showing that the predicted values are very close to the measured width (2–5 nm) of individual nano-scaled twins. Bundles of these nanotwins eventually form micron-sized deformation twins.
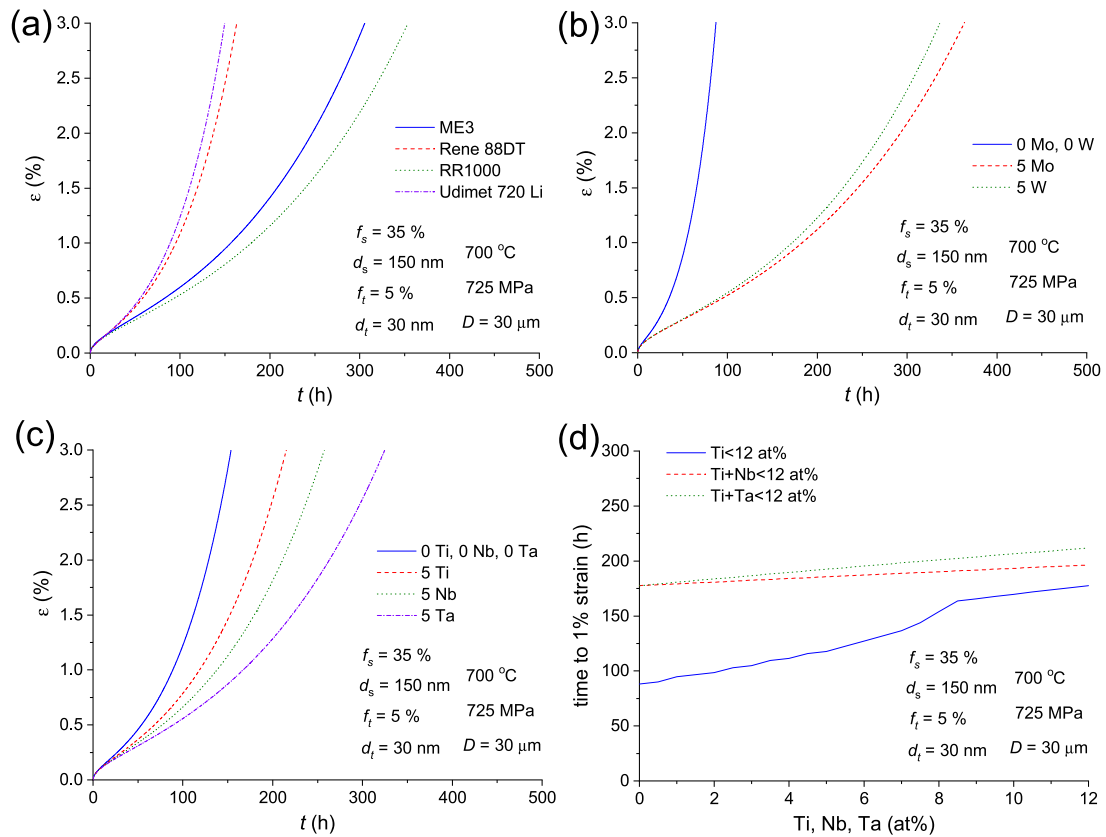
Fig. 7. Chemical composition effects. (a) Comparison in alloy performance for a given creep condition. Effects in the creep response with (b) Mo and W additions in the γ, (c) Ti, Nb and Ta additions in the γ' and (d) time to reach 1% creep strain when modifying the ratios Ti/Nb and Ti/Ta in the γ'. (For interpretation of the references to colour in this figure legend, the reader is referred to the web version of this article.)

The ability of a stacking fault to cut a γ' particle was obtained by performing a force balance at the γ/γ' interface, in a similar fashion as the strong/weak pair coupling model for the critical resolved shear stress (Galindo-Nava et al., 2015), but in this case a stacking fault is exerting the force on the γ' interface leading to an effective cutting length. The stacking fault density rate was proposed in a similar fashion as Dyson's model for creep via dislocation climb, but in the present case the increase in stacking fault density was dictated by the frequency of stacking faults encountering secondary and tertiary γ' precipitates. It was shown that the tertiary γ' delay stacking fault propagation and lower the strain rate via increasing the number of athermal shear events. In addition, the strain and strain rates were proportional to the mobility of the stacking faults within the γ', as short range diffusion dictates the effective mobility of stacking faults in the γ' (Kovarik et al., 2009). The Orowan equation was then used to compute the strain rate, where the stacking fault mobility was proportional to the activation energy for γ' shear and short-range diffusion coefficient of Co and Cr in the γ', as it has been experimentally observed that these elements tend to segregate towards stacking faults to restore local ordering in the γ' (Kovarik et al., 2009). The role of chemical composition was mostly associated to changes in surface energies, *i.e.* γ_{SFE} and γ_{APB}. The model predicted that the effect of γ and γ' partitioning elements in creep lied mostly on controlling γ_{SFE} and γ_{APB}, respectively. It has been reported that stacking fault shear is less frequent as the stacking fault energy increases and the creep strain is mainly governed by dislocation slip (Wang et al., 2015) and the model reflected this by predicting a higher creep rate with higher γ_{SFE}.

The model results were compared against tensile creep tests in several alloys having markedly different compositions and microstructures. Using these results it was possible to compare the individual influence in creep of thermally-activated shear of secondary γ' and the (athermal) shear of small but finely dispersed tertiary γ' particles. For instance, similar creep responses were obtained in alloys with very fine ~ 50 nm secondary (monomodal) γ' as those with (multimodal) coarse secondary γ' but much finer ~ 20 nm tertiary γ'. Similarly, increasing the volume fraction of secondary γ' had a stronger effect in increasing alloy's creep life than when the volume fraction of tertiary γ' increases, due to the thermally-activated processes involved in the former. These results can be useful when designing microstructures for a range of properties, like strength and fatigue, where specific particle size distributions provide the strongest alloys. Although the model succeeded at incorporating several microstructural and compositional effects on creep controlled by stacking fault nucleation and propagation, it also has some limitations. For example, the model predictions did not accurately match every experimental creep curve tested. However, since the main aim of this work is to introduce the first description of stacking fault shear considering several factors indicated previously, we consider that the balance between

model accuracy and features included is very good and the work demonstrates high novelty. In addition, other dislocation-based mechanisms were not considered, such as vacancy-assisted climb or dislocation recovery at higher temperatures, which limits its predictability to temperatures above 750 °C; this could be tackled by incorporating existing models of these processes (Dyson, 2009; Svoboda and Lukáš, 1997) in the creep strain equation (ε_{dis}, Eq. (12)) and estimating the fraction between dislocations dissociating into partials (to form stacking faults) and those gliding/climbing around γ' precipitates (f_{SF}, Eq. (12)). Similarly, the model assumes that tertiary creep is solely associated to dislocation/stacking fault activity, *i.e.* intragranular deformation, and it does not include possible intergranular damage, such as "creep brittleness" with an intergranular fracture mode due to grain boundary sliding (GBS) (Perry, 1974; Wu et al., 2012); the reason for not considering damage is to simplify the present study and focus on microstructural and compositional effects during early stages of creep. Nonetheless, the present model could be useful to understand local strain build up that could lead to the promotion/prevention of GBS effects. In addition, the model is constitutive and does not consider orientation effects possibly altering the nucleation of stacking faults, as these are known to be promoted by specific grain orientations (Karaman et al., 2001); such can be addressed by embedding Eqs. (8) and (12) into a crystal-plasticity finite element analysis (CPFEA) framework to study individual grain deformation using a representative volume element. In addition, micromechanical modelling could be useful to conduct stress analysis at the γ/γ' interface and identify the regions where stacking fault shear dominates over other mechanisms, like dislocation recovery and/or climb. The previous limitations can be addressed in future work.

In summary, the following conclusions can be drawn from this work:

1. A microstructure– and composition–sensitive model for intermediate temperature creep of Ni-based superalloys has been derived. By describing stacking fault evolution within the γ and γ', it was shown that the role of the γ' volume fraction was to increase the critical energy for stacking fault formation, as well as increasing the frequency of shear events, both lowering the creep rate. Similarly, it was obtained that the average size of secondary γ' particles affects the primary and tertiary creep rates, via increasing the stacking fault density and lowering the stacking fault mobility. For the case of alloys with multimodal particle size distributions, it was predicted that tertiary γ' precipitates mostly influence tertiary creep by increasing the frequency of (athermal) shear events that delay stacking fault propagation in between secondary γ' particles. As for the grain size, it was predicted that its main role is on dislocation emission which affects the stacking fault nucleation rate and tertiary creep.

2. It was predicted that one of the main parameters controlling the creep rate is the stacking fault energy in the γ (γ_{SFE}). It was shown that γ_{SFE} had a stronger impact in creep compared to other material parameters like the anti-phase boundary energy. This is due to the γ_{SFE} driving stacking fault nucleation and subsequent shearing in both γ and γ', which increases (or decreases) the creep rate, whereas γ_{APB} featured only in the force balance to shear secondary γ' particles.

3. Effects of chemical composition on alloy's creep life were explored highlighting that Co has a strong influence in lowering the creep strain if it has a concentration high enough (> 15 wt%) to lower the γ_{SFE}. However, elements like Mo and W have stronger effect in lowering γ_{SFE} but they are typically not added in commercial alloys more than $\sim$ 5 at%, hence their impact on creep was not easily identified. As for γ' partitioning elements, Ta showed the strongest effect, followed by Nb and Ti, by increasing γ_{APB} and preventing γ' shearing but their overall potency was not as high as the previously mentioned γ–partitioning elements. The results show how the present model can be used as tool for alloy and microstructure design against creep.

CRediT authorship contribution statement

E.I. Galindo-Nava: Study conception and design, Model development, Analysis and interpretation of results, Writing – original draft. **R. Schlütter:** Study conception and design, Experiments and data collection, Analysis and interpretation of results, Writing – original draft. **O.M.D.M. Messé:** Study conception and design, Experiments and data collection, Analysis and interpretation of results, Writing – original draft. **C. Argyrakis:** Study conception and design, Analysis and interpretation of results, Writing – original draft. **C.M.F. Rae:** Study conception and design, Analysis and interpretation of results, Writing – original draft.

Declaration of competing interest

The authors declare the following financial interests/personal relationships which may be considered as potential competing interests: Enrique Galindo-Nava reports financial support was provided by Royal Academy of Engineering. Catherine Rae reports financial support was provided by Engineering and Physical Sciences Research Council.

Data availability

I have attached source codes as supplementary information.

Acknowledgements

Appendix A. Supplementary data

Supplementary material related to this article can be found online at https://doi.org/10.1016/j.ijplas.2023.103729.

References

Allain, S., Chateau, J., Bouaziz, O., Migot, S., Guelton, N., 2004. Correlations between the calculated stacking fault energy and the plasticity mechanisms in Fe-Mn-C alloys. Mater. Sci. Eng. A 387, 158–162.

Angella, G., Donnini, R., Ripamonti, D., Maldini, M., 2014. The role of particle ripening on the creep acceleration of Nimonic 263 superalloy. MATEC Web Conf. 14, 14001.

Bagot, P., Silk, O., Douglas, J., Pedrazzini, S., Crudden, D., Martin, T., Hardy, M., Moody, M., Reed, R., 2017. An atom probe tomography study of site preference and partitioning in a nickel-based superalloy. Acta Mater. 125, 156–165.

Barba, D., Alabort, E., Garcia-Gonzalez, D., Moverare, J., Reed, R., Jerusalem, A., 2018. A numerical model to predict mechanical properties of Ni-base disk superalloys. Int. J. Plast. 110, 74–98.

Barba, D., Alabort, E., Pedrazzini, S., Collins, D., Wilkinson, A., Bagot, P., Moody, M., Atkinson, C., Jerusalem, A., 2017. On the microtwinning mechanism in a single crystal superalloy. Acta Mater. 135, 314–319.

Bauer, A., Neumeier, S., Pyczak, F., Singer, R., Göken, M., 2012. Creep properties of different γ'-strengthened Co-base superalloys. Mater. Sci. Eng. A 550, 333–341.

Becker, M., Hackenberg, H., 2011. A constitutive model for rate dependent and rate independent inelasticity. Application to IN718. Int. J. Plast. 27, 596–619.

Benyoucef, M., Décamps, B., Coujou, A., Clément, N., 1995. Stacking-fault energy at room temperature of the γ matrix of the MC2 Ni-based superalloy. Phil. Mag. A 71, 907–923.

Bonnet, R., Ati, A., 1991. Evidence for microtwinning as a deformation mechanism in CMSX-2 superalloy. Scripta Metall. Mater. 25, 1553–1556.

Cermak, J., Gazda, A., Rothova, V., 2003. Interdiffusion in ternary Ni_3Al/Ni_3Al-X diffusion couples with X=Cr, Fe, Nb and Ti. Intermetallics 11, 939–946.

Chandra, M., Sondhi, S., 2011. First-principle calculation of stacking fault energies in Ni and Ni-Co alloy. J. Appl. Phys. 109, 103525.

Chang, H., Fivel, M., Strudel, J., 2018. Micromechanics of primary creep in Ni base superalloys. Int. J. Plast. 108, 21–39.

Chang, K.M., Liu, X., 2001. Effect of γ' content on the mechanical behavior of the WASPALOY alloy system. Mater. Sci. Eng. A 308 (1–2), 1–8.

Chatterjee, S., Li, Y., Po, G., 2021. A discrete dislocation dynamics study of precipitate bypass mechanisms in nickel-based superalloys. Int. J. Plast. 145, 103062.

Collins, D., Stone, H., 2014. A modelling approach to yield strength optimisation in a nickel-base superalloy. Int. J. Plast. 54, 96–112.

Connor, L., 2009. The development of a dual microstructure heat treated Ni-base superalloy for turbine disc applications (Ph.D. thesis). University of Cambridge.

Crudden, D., Mottura, A., Warnken, N., Raeisinia, B., Reed, R., 2014. Modelling of the influence of alloy composition on flow stress in high-strength nickel-based superalloys. Acta Mater. 75, 356–370.

Cui, C., Gu, Y., Yuan, Y., Osada, T., Harada, H., 2011. Enhanced mechanical properties in a new Ni-Co base superalloy by controlling microstructures. Mater. Sci. Eng. A 528, 5465–5469.

Cui, C., Tian, C., Zhou, Y., Jin, T., Sun, X., 2012. Dynamic strain aging in Ni base alloys with different stacking fault energy. Superalloys 37–40.

Drexler, A., Fischersworring-Bunk, A., Oberwinkler, B., Ecker, W., Gänser, H., 2018. A microstructural based creep model applied to alloy 718. Int. J. Plast. 105, 62–73.

Dyson, B., 2009. Microstructure based creep constitutive model for precipitation strengthened alloys: theory and application. Mater. Sci. Tech. 25, 213–220.

Freund, L., Messé, O., Barnard, J., Göken, M., Neumeier, S., Rae, C., 2017. Segregation assisted microtwinning during creep of a polycrystalline $L1_2$-hardened co-base superalloy. Acta Mater 123, 295–304.

Friedel, J., 1964. Dislocations. Addison-Wesley, Reading.

Friedel, J., 1977. Sur le fluage par déviation. Rev. Phys. Appl. 12, 1649–1654.

Fu, B., Du, K., Han, G., Cui, C., Zhang, J., 2015. Deformation mechanisms in a Co-rich nickel based superalloy with different size of γ' precipitates. Mater. Letters 152, 272–275.

Galindo-Nava, E., Connor, L., Rae, C., 2015. On the prediction of the yield stress of unimodal and multimodel γ' Nickel-base superalloys. Acta Mater. 98, 377–390.

Galindo-Nava, E., Rae, C., 2016. Microstructure-sensitive modelling of dislocation creep in polycrystalline FCC alloys: Orowan theory revisited. Mater. Sci. Eng. A 651, 116–126.

Galindo-Nava, E., Rivera-Díaz-del-Castillo, P., 2017. Understanding martensite and twin formation in austenitic steels: A model describing TRIP and TWIP effects. Acta Mater. 128, 120–134.

Guimier, A., Strudel, J., 1970. Stacking fault formation and mechanical twinning processes in a nickel-base superalloy during tensile deformation at high temperature. In: Proc. 2nd Int. Conf. Strength Metals and Alloys, Vol. 3. pp. 1145–1149.

Han, G., Jones, I., Smallman, R., 2003. Direct evidence for Suzuki segregation and Cottrell pinning in MP159 superalloy obtained by FEG(S)TEM/EDX. Acta Mater. 51, 2731–2742.

Hayes, R., Unocic, R., Nasrollahzadeh, M., 2015. Creep deformation of Allvac 718Plus. Metall. Mater. Trans. A 46, 218–228.

Humphreys, F., Hatherly, M., 2004. Recrystallization and Related Annealing Phenomena. Elsevier.

Huron, E., Bain, K., Mourer, D., Gabb, T., 2008. Development of high temperature capability P/M disk superalloys. Superalloys 181–189.

Hwang, J., Nag, S., Singh, A., Srinivasa, R., Tiley, J., Fraser, H., Banerjee, R., 2009a. Evolution of the γ/γ' interface width in a commercial nickel base superalloy studied by three-dimensional atom probe tomography. Scr. Mater. 61, 92–95.

Hwang, J., Nag, S., Singh, A., Srinivasa, R., Tiley, J., Viswanathan, G., Fraser, H., Banerjee, R., 2009b. Compositional variations between different generations of γ' precipitates forming during continuous cooling of a commercial nickel-base superalloy. Metall. Mater. Trans. A 40, 3059–3068.

Jackson, P., Reed, R., 1999. Heat treatment of UDIMET 720Li: the effect of microstructure on properties. Mater. Sci. Eng. A 259, 85–97.

Jarrett, R., Tien, J., 1982. Effects of cobalt on structure, microchemistry and properties of a wrought nickel-base superalloy. Metall. Trans. A 13, 1021–1032.

Jones, N., Christofidou, K., Pignatelli, P., Minshull, J., Hardy, M., Stone, H., 2014. Influence of elevated Co and Ti levels on polycrystalline powder processed Ni-base superalloy. Mater. Sci. Tech. 30, 1853–1861.

Kamino, T., Ueki, Y., Hamajima, H., Sasaki, K., Kuroda, K., Saka, H., 1992. Direct evidence for Suzuki segregation obtained by high-resolution analytical electron microscopy. Phil. Mag. Letters 66, 27–31.

Karaman, I., Sehitoglu, H., Chumnlyakov, Y., Maier, H., Kireeva, I., 2001. Extrinsic stacking faults and twinning in Hadfield manganese steel single crystals. Scr. Mater. 44, 337–343.

Karthikeyan, S., Unocic, R., Sarosi, P., Viswanathan, G., Whitis, D., Mills, M., 2006. Modeling microtwinning during creep in Ni-based superalloys. Scr. Mater. 54, 1157–1162.

Kibey, S., Liu, J., Johnson, D., Sehitoglu, H., 2007. Predicting twinning stress in fcc metals: linking twin-energy pathways to twin nucleation. Acta Mater. 55, 6843–6851.

Kienl, C., León-Cázares, F., Rae, C., 2022. Deformation twinning during high temperature compression tests of the Ni-base superalloy ATI 718plus®. Acta Mater. 225, 1359–6454.

Kim, I., Choi, B., Hong, H., Yoo, Y., Jo, C., 2011. Anomalous deformation dehavior and twin formation of Ni-base superalloys at the intermediate temperatures. Mater. Sci. Eng. A 528, 7149–7155.

Kim, Y., Kim, D., Kim, H., Oh, C., Lee, B., 2016. An intermediate temperature creep model for Ni-based superalloys. Int. J. Plast. 79, 153–175.

Kim, Y., Kim, D., Kim, H., Yoon, E., Lee, Y., Oh, C., Lee, B., 2018. A numerical model to predict mechanical properties of Ni-base disk superalloys. Int. J. Plast. 110, 123–144.

Koizumi, Y., Nukaya, T., Suzuki, S., Shingo, K., Li, Y., Matsumoto, H., Sato, S., Tanaka, Y., Chiba, A., 2012. Suzuki segregation in Co-Ni-based superalloy at 973 J: An experimental and computational study by phase-field simulation. Acta Mater. 60, 2901–2915.

Koizumi, Y., Suzuki, S., Otomo, T., Kurosu, S., Li, Y., Matsumoto, H., Chiba, A., 2011. Phase-field simulation of segregation to stacking fault (Suzuki effect) in Co-Ni-based superalloy. TMS Supp. Proc.: Mater. Fabr., Prop., Charact., Model. 2, 409–416.

Kolbe, M., 2001. The high temperature decrease of the critical resolved shear stress in nickel-base superalloys. Mater. Sci. Eng. A 319, 383–387.

Kovarik, L., Unocic, R., Li, J., Sarosi, P., Shen, C., Wang, Y., Mills, M., 2009. Microtwinning and other shearing mechanisms at intermediate temperatures in Ni-based superalloys. Prog. Mater. Sci. 54, 839–873.

Legros, M., Clément, N., Caron, P., Coujou, A., 2002. In-situ observation of deformation micro mechanisms in a rafted γ/γ' superalloy at 850 °C. Mater. Sci. Eng. A 337, 160–169.

Li, J., 1963. Petch relation and grain boundary sources. Trans. Metall. Soc. AIME 277, 239–247.

Locq, D., Caron, P., Raujol, S., Pettinari-Sturmel, F., Coujou, A., Clément, N., 2004. On the role of tertiary γ' precipitates in the creep behaviour at 700 °C of a PM disk superalloy. Superalloys 179–187.

Manonukul, A., Dunne, F., Knowles, D., 2002. Physically-based model for creep in nickel-base superalloy C263 both above and below the gamma solvus. Acta Mater. 50, 2917–2931.

Meng, Z., Sun, G., Li, M., 1984. The strengthening effect of tantalum in nickel-base superalloys. Superalloys 563–572.

Messe, O., 2015. Studies of the Fatigue Behaviour in Coarse Grained RR1000 (Ph.D. thesis). University of Cambridge.

Mishin, Y., 2004. Atomistic modeling of the γ and γ'-phases of the Ni-Al system. Acta Mater. 52, 1451–1467.

Monni, F., 2021. Grain Boundaries and Creep Deformation Mechanisms in a High Performance Nickel-Based Superalloy (Ph.D. thesis). University of Cambridge.

Nabarro, F., 2004. Do we have an acceptable model of power-law creep? Mater. Sci. Eng. A 387, 659–664.

Naeita, N., Takamura, J., 1974. Deformation twinning in silver- and copper-alloy crystals. Phil. Mag. 29, 1001–1028.

Olson, G., Cohen, M., 1976. A general mechanism of martensitic nucleation: Part I. General concepts and the FCC→HCP transformation. Metall. Trans. A 7, 1897–1904.

Olson, G., Jou, H., Jung, J., Sebastian, J., Misra, A., Locci, I., Hull, D., 2008. Precipitation model validation in 3rd generation aeroturbine disc alloys. Superalloys 923–932.

Perry, A., 1974. Cavitation in creep. J. Mater. Sci. 9, 1016–1039.

Pierce, D., Jiménez, J., Bentley, J., Raabe, D., Oskay, C., Witting, J., 2014. The influence of manganese content on the stacking fault and austenite/ϵ-martensite interfacial energies in Fe-Mn-(Al-Si) steels investigated by experiment and theory. Acta Mater. 68, 238–253.

Pollock, T., Argon, A., 1992. Creep resistance of CMSX-3 nickel base superalloy single crystals. Acta Metall. Mater. 40, 1–30.

Rae, C., Reed, R., 2007. Primary creep in single crystal superalloys: Origins mechanisms and effects. Acta Mater. 55, 1067–1081.

Rae, C., Zhang, L., 2009. Primary creep in single crystal superalloys: some comments on effects of composition and microstructure. Mater. Sci. Tech. 25, 228–235.

Ram, F., Li, Z., Zaefferer, S., Hafez Haghighat, S.M., Zhu, Z., Raabe, D., Reed, R.C., 2016. On the origin of creep dislocations in a Ni-base, single-crystal superalloy: An ECCI, EBSD, and dislocation dynamics-based study. Acta Mater. 109, 151–161.

Reed, R., 2006. The Superalloys: Fundamentals and Applications. Cambridge University Press.

Shang, S., Zacherl, C., Fang, H., Wang, Y., Du, Y., Liu, Z., 2012. Effects of alloying element and temperature on the stacking fault energies of dilute Ni-base superalloys. J. Phys.: Condens. Matter 24, 505403.

Smith, T., Unocic, R., Deutchman, H., Mills, M., 2006. Creep deformation mechanism mapping in nickel base disk superalloys. Mater. High Temp. 33, 372–383.

Svoboda, J., Lukáš, P., 1997. Modelling of recovery controlled creep in nickel-base superalloy single crystals. Acta Mater. 45, 125–135.

Svoboda, J., Lukáš, P., 1998. Model of creep in ⟨001⟩-oriented superalloy single crystals. Acta Mater. 46, 3421.

Svoboda, J., Lukáš, P., 2000. Creep deformation modelling of superalloy single crystals. Acta Mater. 48, 2519.

Talonen, J., Hänninen, H., 2007. Formation of shear bands and strain-induced martensite during plastic deformation of metastable austenitic stainless steels. Acta Mater. 6108–6118, 55.

Tian, C., Han, G., Cui, C., Sun, X., 2014. Effects of stacking fault energy on the creep behaviors of Ni-base superalloy. Mater. Des. 64, 316–323.

Tschopp, M., McDowell, D., 2008. Grain boundary dislocation sources in nanocrystalline copper. Scr. Mater. 58 (4), 299–302.

Unocic, R., Viswanathan, G., Sarosi, P., Karthikeyan, S., Li, J., Mills, M., 2008. Mechanisms of creep deformation in polycrystalline Ni-base disk superalloys. Mater. Sci. Eng. A 483, 25–32.

Unocic, R., Zhou, N., Kovarik, L., Shen, C., Wang, Y., Mills, M., 2011. Dislocation decorrelation and relationship to deformation micro twins during creep of a γ' precipitate strengthened Ni-based superalloy. Acta Mater. 59, 7325–7339.

Vamsi, K., Karthikeyan, S., 2012. Effect of off-stoichiometry and ternary additions on planar fault energies in Ni$_3$Al. Superalloys 521–530.

Viskari, L., Stiller, K., 2011. Atom probe tomography of Ni-base superalloys Allvac 718Plus and Alloy 718. Ultramicroscopy 111, 652–658.

Viswanathan, G., Sarosi, P., Herny, M., Whitis, D., Milligan, W., Mills, M., 2005. Investigation of creep deformation mechanisms at intermediate temperatures in René 88 DT. Acta Mater. 53, 3041–3057.

Viswanathan, G., Shi, R., Genc, A., Vorontsov, V., Kovarik, L., Rae, C., Mills, M., 2015. Segregation at stacking faults within the γ' phase of two Ni-base superalloys following intermediate temperature creep. Scr. Mater. 94, 5–8.

Wang, W., Jin, T., Jia, J., Liu, J., Hu, Z., 2015. Effects of cobalt on creep rupture properties and dislocation structures in nickel base superalloys. Mater. Sci. Eng. A 624, 220–228.

Wu, X., Williams, S., Gong, D., 2012. A true-stress creep model based on deformation mechanisms for polycrystalline materials. J. Mater. Eng. Perform. 21, 2255–2262.

Wu, R., Zaiser, M., Sandfeld, S., 2017. PA continuum approach to combined γ/γ' evolution and dislocation plasticity in nickel-based superalloys. Int. J. Plast. 95, 142–162.

Wu, R., Zhang, Y., 2022. Phase-field, dislocation based plasticity and damage coupled model: Modelling and application to single crystal superalloys. Int. J. Plast. 157, 103376.

Xia, P., Yu, J., Sun, X., Guan, H., Hu, Z., 2007. Influence of thermal exposure on γ' precipitation and tensile properties of DZ951 alloy. Mater. Charact. 58 (7), 645–651.

Xu, Y., Qi, D., Du, K., Cui, C., Ye, H., 2014. Stacking fault effects on dynamic strain raging in a Ni-Co-based superalloy. Scr. Mater. 87, 37–40.

Yuan, Y., Gu, Y., Cui, C., Osada, T., Zhong, Z., Tetsui, T., Yokokawa, T., Harada, H., 2011a. Influence of Co content on stacking fault energy in Ni-Co base disk superalloys. J. Mater. Res. 26, 2833–2837.

Yuan, Y., Gu, Y., Cui, C., Osada, T., Tetsui, T., Yokokawa, T., Harada, H., 2011b. Creep mechanisms of U720Li disc superalloy at intermediate temperature. Mater. Sci. Eng. A 528, 5106–5111.

Yuan, Y., Gu, Y., Zhong, Z., Osada, T., Cui, C., Tetsui, T., Yokokawa, T., Harada, H., 2012. Creep mechanisms of a new Ni-Co-base disc superalloy at an intermediate temperature. J. Micros. 248, 34–41.

Zhang, J., Li, J., Jin, T., Sun, X., Hu, Z., 2010. Effect of Mo concentration on creep properties of a single crystal nickel-base superalloy. Mater. Sci. Eng. A 527, 3051–3056.

Zhao, P., Mills, M., Sang, Y., Niezgoda, S., 2018. A homogenized primary creep model of nickel-base superalloys and its application to determining micro-mechanistic characteristics. Int. J. Plast. 110, 202–219.

Zhi'an, Y., Yaotian, X., Changxu, S., 1988. The role of cobalt in the high temperature creep of γ'-strengthened Nickel-based superalloys. Mater. Sci. Eng. A 101, 65–73.

Zhu, Z., Basoalto, H., Warnken, N., Reed, R., 2012. A model for the creep deformation behaviour of nickel-based single crystal superalloys. Acta Mater. 60, 4888–4900.